Hidrovo, C., Goodson, K.E., 2008, "Active Microfluidic Cooling of Integrated Circuits," in Electrical, Optical, and Thermal Interconnections for 3D Integrated Systems, J. Meindl and M. Bakir, eds., Artech, Boston, pp. 293-330

CHAPTER 10

Active Microfluidic Cooling of Integrated Circuits

Carlos H. Hidrovo and Kenneth E. Goodson

10.1 Introduction

The thermal management of high heat fluxes is a critical roadblock in the way of higher-performance microelectronics. The ongoing reduction in microtransistor size translates into heat fluxes comparable to those encountered in nuclear reactions and rocket nozzles, but under much severer temperature constraints. Although the average heat flux may remain in the vicinity of 100 to 300 W/cm^2, the peak heat flux at localized hot spots may approach or exceed 1 kW/cm^2. In order to handle these heat fluxes properly at lower operating temperatures, integrated cooling technologies that remove heat closer to the source are required. Microfluidic cooling in a heat sink built within or attached directly to the silicon chip is one route to address this problem. Three primary microfluidic technologies have the potential to accommodate this very large heat flux. These include microjet impingement, spray cooling, and microchannel heat sinks [1]. Microjet impingement relies on the use of a high-speed liquid jet that emerges from a nozzle to reduce thermal boundary-layer thicknesses and increase convection coefficients at the incident surface. Despite being one of the leading cooling technologies, microjet impingement has serious drawbacks in terms of fluid recovery for open systems and temperature uniformity. Therefore, intricate architectures using multiple microjets and specially designed outlet ports are needed. This leads to designs that are highly optimized for very specific thermal operating conditions and are therefore not robust to time and spatially varying thermal loads. Similar to microjet impingement, spray cooling relies on the impingement of liquid onto the heated surface. Spray cooling relies on a blanket of liquid droplets rather than a continuous liquid jet striking the heated source, providing better surface coverage and temperature uniformity. Furthermore, rather than relying on the convective transport capabilities of the thin liquid film formed when the droplets hit the surface, spray cooling is achieved through the evaporation of the aforementioned film. The latent heat associated with the phase change translates into lower surface-temperature requirements, another advantage over microjet impingement cooling. This makes spray cooling one of the leading contenders in the race to achieve heat-flux removal values exceeding 1 kW/cm^2. However, it has serious drawbacks in terms of the pressures required to achieve proper spray droplet breakup and the distribution needed to exploit the cooling potential of this technology fully.

Microchannel heat sinks have received much attention from the research community over nearly three decades. The seminal paper by Tuckerman and Pease [2] demonstrated a microchannel heat sink capable of removing 790 W/cm^2 with a temperature rise of 71°C using water at a flow rate of 516 mL/min and just over 2 atm of required pressure head. Their work has been followed by a number of studies of single- and two-phase microchannel flows, including those by Phillips et al. [3], Samalam [4], Peng and Wang [5], Bowers and Mudawar [6], Peles et al. [7], Lin et al. [8], Qu and Mudawar [9], and Zhang et al. [10], as well as several comprehensive review articles on the topic [11–14]. As the semiconductor industry and research community move toward the realization of 3-D IC, packaging constraints become the primary consideration when choosing a cooling technology that can allow seamless integration with these novel architectures. Both microjet impingement and spray cooling require stacking of several fabrication layers for the creation of the nozzle structures and to achieve the required separation for proper jet and spray formation. For this reason, and given the maturity of this technology, this chapter focuses on microchannel heat sink cooling since it is at the forefront of implementation feasibility for 3-D IC applications. In Section 10.2 we discuss the fundamentals of single-phase flow and convective heat transfer. We then proceed to delineate the most salient features of two-phase flow boiling, as they pertain to microchannel cooling, in Section 10.3. Section 10.4 is devoted to the topic of fluid flow and convection modeling in microchannels, paying particular attention to the two-phase flow boiling regime, where, for the most part, existing macroscale models are not applicable. The substantial pumping requirements associated with microchannel flow, in the context of cooling performance, are covered in Section 10.5. Intrinsically related to the large pressure drops associated with microchannel cooling is the design of optimal and novel microchannels network architectures that can lessen the effect of this detrimental characteristic. This is explored in Section 10.6, particularly from the perspective of 3-D IC. Section 10.7 concludes the chapter with an outlook on future and promising technologies that might prove key in the successful development and commercialization of next generation microchannel cooling systems.

Before proceeding, a clarification note: we will employ the term *microchannel* to designate indistinguishable**<AQ: edit to reverse order of designate and indistinguishable here okay?>** channels with characteristic cross-sectional length scales on the order of micrometers, regardless of geometry. It is not uncommon to associate the term microchannel instinctively with a rectangular cross section since this is the most prevalent type of microchannel geometry. However, depending on the fabrication procedures and processes, one can attain other types of cross-sectional geometries, including semicircular and triangular, just to mention two.

10.2 Single-Phase Flow Cooling

The original microchannel heat sink concept introduced by Tuckerman and Pease used single-phase liquid water. In this section we discuss the fundamentals behind single-phase flow convection. Continuum theory can be used to describe the flow of liquids, such as water and other commonly employed refrigerants (water is generally chosen as the working fluid in microchannel heat sink cooling systems due to its

superb thermal properties and benign environmental characteristics), and their behavior in mini- and microchannels [15]. This is not necessarily the case for gases, where the Knudsen number (Kn, a dimensionless number defined as the ratio of the molecular mean free path to a representative physical length scale) can approach values above one depending on the microchannel characteristic dimension. However, for microchannels with values of the hydraulic diameter greater than 10 μm, air and water-vapor behavior can be treated by the classical continuum theory near atmospheric conditions. As such, we will omit treatment of rarefaction effects in single-phase gas flows and concentrate instead on liquid flows, only noting that for rarefied gas flows, the Nusselt number (Nu)**<AQ: edit okay?>** and therefore the heat-transfer coefficient are reduced when compared to their continuum counterparts [16].

Any discussion of single-phase-flow forced-convection cooling needs to start with the fundamental fluid mechanics principles governing the flow. In what follows, we restrict our treatment to circular cross section microchannels. Although most cooling microchannels have rectangular cross sections, the fundamental flow physics and relevant concepts between the two geometries are unequivocally equivalent. The relative simplicity of the flow solutions for the circular cross section microchannel favors its use for the illustrative purposes of this section.

10.2.1 Laminar Flow Fundamentals

The simplest and most basic form of internal flow is that of incompressible, fully developed, steady-state, single-phase laminar flow through an axisymmetric uniform circular duct for a Newtonian fluid. Solution of the Navier-Stokes and continuity equations for this type of flow gives rise to the well-known Hagen-Poiseuille parabolic velocity profile (Figure 10.1).

$$u = -\frac{1}{4\mu}\frac{dp}{dx}\left(R^2 - r^2\right) \tag{10.1}$$

The existence of an implicit analytical solution for the velocity profile as a function of pressure gradient and duct geometry lends itself to a simple formulation relating pressure drop and flow rate in a circular tube, the quantities of interest for

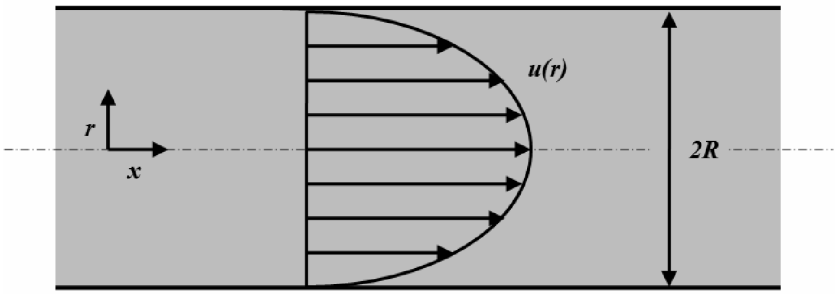

Figure 10.1 Parabolic velocity profile for fully developed laminar flow in a circular cross section tube. The pressure drop balances the shear stress at the wall, which is constant for fully developed flow and proportional to the velocity gradient at the wall.

the designer. Integration of the velocity profile over the area of the duct gives rise to the following equation relating pressure gradient and volumetric flow rate:

$$-\frac{dp}{dx} = \frac{8\mu Q}{\pi R^4} = \frac{8\mu u_{avg}}{R^2} \tag{10.2}$$

For a duct of length L, we have

$$\Delta p = \frac{8\mu QL}{\pi R^4} = \frac{8\mu u_{avg} L}{R^2} \tag{10.3}$$

However, most internal flows do not lend themselves to implicit analytical velocity profiles and corresponding simple formulations for the relationship of pressure drop to volume flow rate. In these instances an alternative formulation more practical for design purposes must be used. One such approach employs the friction coefficient, or Fanning friction factor, which is defined as the ratio of the wall shear stress to the dynamic pressure:

$$C_f = \frac{\tau_w}{(1/2)\rho u_{avg}^2} \tag{10.4}$$

A force balance on an infinitesimal circular fluid element of length dx requires that the force due to pressure difference be opposed by an equal but opposite direction shear-stress force acting against the flow. This can be explained using

$$\pi R^2 dp = 2\pi R dx \tau_w \tag{10.5}$$

and

$$\frac{dp}{dx} = \frac{2\tau_w L}{R} \tag{10.6}$$

Again, for a duct of length L, we have

$$\Delta p = \frac{2\tau_w L}{R} \tag{10.7}$$

Substituting (10.4) into (10.7), we have

$$\Delta p = \frac{2C_f (1/2)\rho u_{avg}^2 L}{R} = \frac{C_f \rho u_{avg}^2 L}{R} \tag{10.8}$$

Comparing (10.3) and (10.8), we have

$$C_f = \frac{8\mu}{\rho u_{avg} R} = \frac{16\mu}{\rho u_{avg} D} = \frac{16}{\mathrm{Re}_D} \tag{10.9}$$

Thus, the Fanning friction factor is inversely proportional to the flow Re through a proportionality constant, in this case 16, which is dependent on the flow-velocity profile. In the case of incompressible, fully developed, steady-state, single-phase laminar flows for Newtonian fluids, it is only dependent on flow-channel geometry. Thus, (10.9) can be generalized for any arbitrary channel geometry as

$$C_f = \frac{Po}{\mathrm{Re}_{D_h}} \tag{10.10}$$

where the circular tube diameter D has been replaced by the hydraulic diameter D_h, which is given by

$$D_h = \frac{4A_c}{P_w} \tag{10.11}$$

The constant C_fRe product is known as the Poiseuille number (Po), and as stated before, it is only a function of channel geometry. Po correlations and values for different channel geometries can be found in authoritative books, such as that from Shah and London [17] (for rectangular cross sections it ranges from 14.23, for a square duct with aspect ratio of one, to 24, in the limiting case of two infinite parallel plates or aspect ratio of zero). The generalized pressure-drop equation can now be stated as

$$\Delta p = \frac{2C_f \rho u_{avg}^2 L}{D_h} \tag{10.12}$$

It is important to explore the underlying implications that these pressure correlations have. Equations (10.10) and (10.12) can be rearranged to provide a general correlation between pressure drop and volumetric flow rate:

$$\Delta p = \frac{8Po\mu QL}{D_h^3 P_w} \tag{10.13}$$

If we compare (10.3) and (10.13), it is apparent that for a given fluid flow rate, the pressure drop is inversely proportional to the fourth power of the channel characteristic length scale (this is somewhat softened toward a third power inverse dependence for very high-aspect-ratio channels by the wetted perimeter term). This has detrimental implications for microchannel flow as the required pressure drops can be quite substantial.

10.2.2 Entrance Effects: Developing Flow and Sudden Contraction and Expansion

The previous section treatment is applicable only to fully developed flows where the velocity profiles remain constant and are not a function of axial position. In reality, internal flows require a finite length of duct before reaching fully developed condi-

tions. As the flow enters the channel, the velocity profile is in constant change as the effects of the wall are propagated into the bulk of the flow (Figure 10.2). Under the assumption of uniform velocity conditions at the entrance, the hydrodynamic entrance length is given by

$$\frac{L_h}{D_h} = 0.05\,\mathrm{Re} \tag{10.14}$$

Depending on flow conditions and overall channel length, the entrance effects can be quite substantial and need to be accounted for. This can be particularly true for microchannels, whose lengths can be relatively short to lessen the toll on pressure drop already imposed by their cross-sectional area, as discussed before. Pressure-drop effects due to the entrance can be accounted for using an apparent Fanning friction factor, which embodies both frictional losses in the entrance and fully developed regions [18]:

$$\Delta p = \frac{2C_{f,app}\rho u_{avg}^2 x}{D_h} \tag{10.15}$$

This equation evaluates the pressure drop as a function of position x from the entrance of the channel. The difference between apparent and fully developed friction factor over a distance x can be expressed in terms of a pressure defect or incremental pressure-drop number, given by

$$K(x) = \left(C_{f,app} - C_f\right)\frac{4x}{D_h} \tag{10.16}$$

$K(x)$ accounts for the additional pressure drop due to momentum change and accumulated increment in wall shear stress in the developing region (Figure 10.2). Therefore, the total pressure drop can be expressed as

$$\Delta p = \frac{2Po\mu u_{avg} x}{D_h^2} + K(x)\frac{\rho u_{avg}^2}{2} \tag{10.17}$$

For $x = L_h$, the incremental pressure defect takes on a constant value of $K(\infty)$. Shah and London [17] postulated the following equation for $K(x^+)$ in circular tubes:

$$K(x^+) = 13.76(x^+)^{1/2} + \frac{1.25 + 64x^+ - 13.76(x^+)^{1/2}}{1 + 0.00021(x^+)^{-2}} - 64x^+ \tag{10.18}$$

where x has been replaced by the dimensionless axial distance x^+ given by

$$x+ = \frac{x}{D_h\,\mathrm{Re}} \tag{10.19}$$

Chen [19] proposed the following correlation for $K(\infty)$ in circular tubes

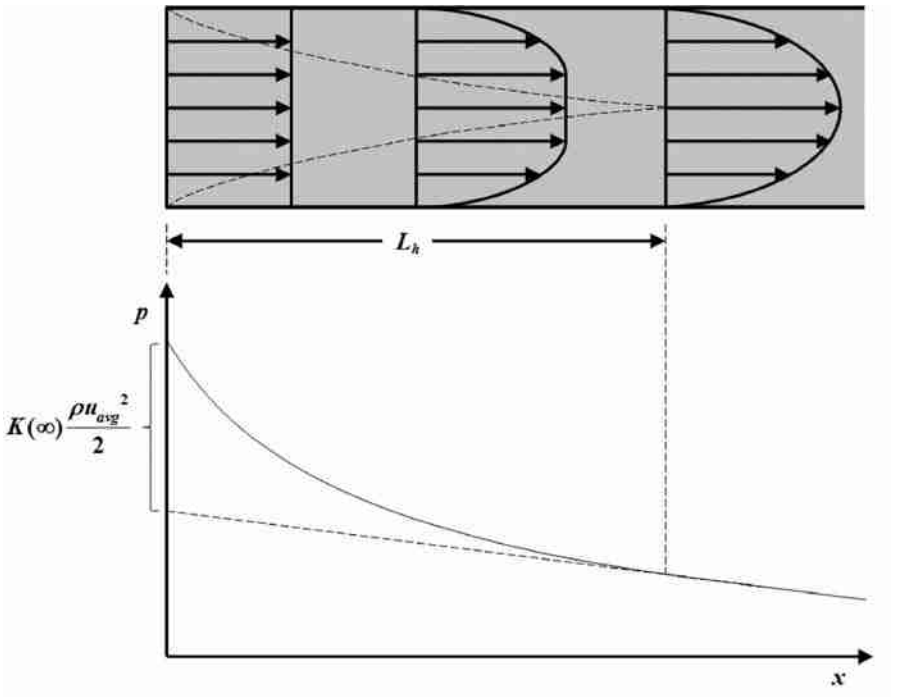

Figure 10.2 Developing velocity profile and pressure drop in the entry region of a circular cross section channel. For $x > L_h$, the flow is fully developed, and the pressure drop is linear. In the developing region, the pressure drop is nonlinear due to momentum change and accumulated increment in wall shear stress. Both of these effects are captured in terms of a pressure defect, $K(x)$, defined as the difference between the actual pressure drop and the fully developed equivalent pressure drop for a given length.

$$K(\infty) = 1.20 + \frac{38}{\mathrm{Re}} \tag{10.20}$$

For further pressure-defect correlations applicable to different channel geometries, the reader is again referred to Shah and London [17].

In addition to entrance-length effects, it is also important to consider other effects related to inlet and outlet ancillaries. These are called "minor losses" and can include the sudden contraction usually encountered at the microchannel inlet, the sudden expansion usually encountered at the microchannel outlet, and bends encountered in the system. All these can be accounted for through the use of loss coefficients K_c, K_e, and K_{90}, respectively, such that the overall pressure drop encountered in a microchannel heat sink system can be expressed as [18]:

$$\Delta p = \frac{\rho u_m^2}{2}\left[\left(A_c / A_p\right)^2 \left(2K_{90}\right) + \left(K_c + K_e\right) + \frac{4C_{f,app}L}{D_h}\right] \tag{10.21}$$

or equivalently

$$\Delta p = \frac{\rho u_m^2}{2}\left[\left(A_c / A_p\right)^2 \left(2K_{90}\right) + \left(K_c + K_e\right) + \frac{4C_f L}{D_h} + K(x)\right] \tag{10.22}$$

10.2.3 Turbulent Flow

Turbulence yields chaotic and stochastic flow behavior. Turbulent flow is characterized by rapid variations (locally and globally) in velocity and pressure in both space and time. It arises under conditions in which flow inertial forces are much larger than viscous forces and therefore dominate. The relative prevalence of these two forces is quantified through the Reynolds number (Re). For internal flows, transition from laminar to turbulent behavior occurs at Re ~ 2,300.

Due to the chaotic nature of the velocity field in turbulent flows, analytical or even numerical calculation of a generalized expression for the friction factor is nearly impossible. It is widely agreed, however, that the correlation derived by Prandtl in 1935 provides a good approximation of the Darcy friction factor for fully developed turbulent flow in a smooth circular channel [20]:

$$\frac{1}{\sqrt{f}} = 2.\log\left(\mathrm{Re}\sqrt{f}\right) - 0.8 \tag{10.23}$$

where the Darcy friction factor is given by

$$f = 4C_f \tag{10.24}$$

Other expressions exist that account for both the developing and fully developed regions and noncircular geometries [18, 20]. In addition, pressure drop in turbulent flow in ducts is greatly influenced by the roughness of the channel walls. Several correlations exist that take surface roughness effects into account through the use of a relative roughness term, ε/D_h (where ε is the absolute surface roughness), in the friction-factor formulation. Among them is the Colebrook equation, which provides a good representation of the Darcy friction factor for turbulent flow in circular tubes as depicted in the widely used Moody chart [20]:

$$\frac{1}{\sqrt{f}} = -2.0\log\left(\frac{\varepsilon / D}{3.7} + \frac{2.51}{\mathrm{Re}\sqrt{f}}\right) \tag{10.25}$$

10.2.4 Steady-State Convective Heat-Transfer Equations: Constant Heat Flux and Constant-Temperature Boundary Conditions

We start the analysis of internal single-phase heat-transfer flow by introducing two key concepts. The first one is the thermal entry length. Steady-state, fully developed thermal conditions refer to those conditions in which the flow thermal (nondimensional temperature) profile is not a function of axial distance along the tube. Internal flows require a finite length of duct before reaching fully developed thermal conditions. As the flow enters the channel, the temperature profile is in constant change as the thermal effects of the wall are propagated into the bulk of the flow. Under the assumptions of uniform temperature with fully developed velocity-profile conditions at the entrance, the thermal entrance length is given by

$$\frac{L_t}{D_h} = 0.05\,\mathrm{Re}\,\mathrm{Pr} \tag{10.26}$$

where Pr compares viscous (momentum) diffusivity to thermal diffusivity and is therefore a ratio of how quickly the momentum (velocity) boundary layer develops in relationship to the thermal (temperature) boundary layer.

The second key concept is that of the mixed mean bulk-flow temperature. Instead of representing the mean or average value for the spatial temperature profile, the mixed mean bulk-flow temperature is defined in terms of the thermal energy transported by the fluid as it moves past a cross section of tube. As such, it is not only dependent on the temperature profile but also on the velocity profile, as the energy transport is a function of temperature (energy measure) and mass flow rate (flow advection measure). The mixed mean bulk-flow temperature T_m is defined as

$$T_m = \frac{\int_{A_c} \rho u c_v T dA_c}{\dot{m} c_v} = \frac{\int_{A_c} \rho u T dA_c}{\dot{m}} \text{ for constant } c_v \tag{10.27}$$

As can be seen from (10.27), the mixed mean temperature is the temperature that provides the same amount of energy transport by advection under a uniform temperature field as that transported by the actual flow with its velocity and temperature profiles.

The mixed mean temperature is used as the reference temperature for internal flows in Newton's law of cooling, which relates heat transfer to a convective heat-transfer coefficient and two reference temperatures. Thus,

$$q_s'' = h(T_s - T_m) \tag{10.28}$$

Due to their nature, internal flows are well suited to a fixed control volume, open system thermodynamic energy balance analysis. The difference in advection energy transport between inlet and outlet must be equal to the heat transfer and shaft work done on the fluid. Since there is no shaft work in simple pipe flow, a basic energy balance yields

$$q_{conv} = \dot{m} c_p (T_{m,o} - T_{m,i}) \tag{10.29}$$

Equation (10.29) is a general and powerful expression that applies to all internal heat-transfer flows irrespective of thermal or fluid flow conditions. An exception arises for incompressible flows when the pressure gradient is extremely large, in which case (10.29) is modified as

$$q_{conv} = \dot{m}\left[c_v (T_{m,o} - T_{m,i}) + \frac{p_o - p_i}{\rho}\right] \tag{10.30}$$

However, for the purposes of this chapter and in most microchannel cooling applications, (10.29) is valid. By casting and combining (10.28) and (10.29) in differential form, the following differential equation for the mean mixed temperature behavior as a function of axial location is obtained:

$$dq_{conv} = \dot{m} c_p dT_m = q_s'' P dx = h(T_s - T_m) P dx \tag{10.31}$$

$$\frac{dT_m}{dx} = \frac{h(T_s - T_m)P}{\dot{m}c_p} \tag{10.32}$$

Equation (10.32) provides the framework for the two fundamental types of internal flow convective heat transfer: constant surface heat flux and constant surface temperature.

Under constant surface heat flux, we can rewrite (10.32) as

$$\frac{dT_m}{dx} = \frac{q_s''P}{\dot{m}c_p} \neq f(x) \text{ (i.e., not a function of } x) \tag{10.33}$$

and therefore

$$T_m(x) = T_{m,i} + \frac{q_s''P}{\dot{m}c_p}x \tag{10.34}$$

In other words, under constant surface heat flux, the bulk mixed mean temperature increases linearly as a function of axial location. This applies irrespective of whether we have fully developed conditions or not.

For constant surface-temperature conditions, derivation of the bulk mixed mean temperature dependence on axial location is slightly more involved but still straightforward, leading to the following result [21]:

$$\frac{T_s - T_m(x)}{T_s - T_{m,i}} = \exp\left(-\frac{Px}{\dot{m}c_p}\bar{h}\right) \tag{10.35}$$

where

$$\bar{h} = \frac{1}{L}\int_0^L h(x)dx \tag{10.36}$$

is the average heat-transfer coefficient over the tube length.

Equation (10.35) depicts an exponential behavior of T_m as it tends toward a limiting value of T_s. Just as in the case of (10.34), (10.35) is a general equation that applies to all internal flows under constant surface temperature, irrespective of other flow conditions. However, there is still specificity related to each particular flow in terms of the heat-transfer coefficient, which influences the exponential behavior of the fluid mixed mean temperature. The same can be said for the case of constant surface heat flux. Although (10.34), and thus the flow mixed mean temperature, is independent of the convective heat-transfer coefficient, the surface temperature on the other hand is directly dependent on the value and behavior of the convective heat-transfer coefficient. The dependence of the convective heat-transfer coefficient on flow conditions is clearly illustrated by looking at its definition along with Fourier's law of heat conduction:

$$q_s'' = h(T_s - T_{char}) = -k_f \left.\frac{\partial T}{\partial n}\right|_{n=0} \tag{10.37}$$

$$h = \frac{-k_f \left.\frac{\partial T}{\partial n}\right|_{n=0}}{(T_s - T_{char})} \tag{10.38}$$

where T_{char} is the characteristic temperature in Newton's law of cooling (free stream temperature in external flows and mixed mean temperature in internal flows), and n is the direction normal to the surface. Equation (10.38) is a general equation that relates the convective heat-transfer coefficient to the heat conduction in the flow at the surface. Since the heat conduction in the flow at the surface is dependent on the flow temperature profile, the convective heat-transfer coefficient is therefore dependent on the flow thermal conditions.

For circular tubes with laminar flow under fully developed thermal and velocity-profile conditions, it can be shown that for the case of constant surface heat flux, the convective heat-transfer coefficient is equal to [21]

$$h = \frac{48}{11}\left(\frac{k_f}{D}\right) \tag{10.39}$$

It is usually more customary to express convective heat transfer in terms of the nondimensional Nusselt (Nu) number, which compares heat transfer by fluid convection to heat transfer by fluid thermal diffusion (equivalently, it can be thought of as a dimensionless temperature profile within the flow). In this case,

$$Nu = \frac{hD}{k_f} = 4.36 \tag{10.40}$$

A more elaborate analysis produces a similar result for the case of constant wall temperature, for which [21]

$$Nu = \frac{hD}{k_f} = 3.66 \tag{10.41}$$

Calculating convective heat-transfer coefficients under entry-length conditions is a more complicated problem, and two cases need to be considered. In the first case, we have fully developed velocity-profile conditions with a developing temperature profile. This is akin to starting the heat transfer after an unheated section beyond the tube inlet once the velocity profile has reached fully developed conditions. It is also representative of the flow of fluids with large Pr, where the velocity-profile entry length is much smaller than the thermal entry length. The second case considers concurrent momentum and thermal entry-length conditions, with both the velocity and temperature profiles simultaneously changing. Here, we present average Nu correlations for the two cases described above under constant surface-temperature conditions, given that the average convective heat-transfer coefficient is a required parameter in (10.35):

$$\overline{Nu} = 3.66 + \frac{0.0668(D/L)\mathrm{RePr}}{1 + 0.04\left[(D/L)\mathrm{RePr}\right]^{2/3}} \tag{10.42}$$

$$\overline{Nu} = 1.86\left(\frac{\mathrm{Re}\,\mathrm{Pr}}{L/D}\right)^{1/3}\left(\frac{\mu}{\mu s}\right)^{0.14} \tag{10.43}$$

where μ_s is the viscosity of the fluid at the surface temperature. All other properties in (10.42) and (10.43) are evaluated at the average value of the mean temperature, $T_m = (T_{m,i} + T_{m,o})/2$. Turbulence increases convective heat transfer due to the higher momentum transport associated with this type of flow regime. Several heat-transfer correlations exist for turbulent flow. The reader is referred to the treatise by Shah and London [17] and the textbook by Incropera et al. [21]. Here, we present two of the most widely used:

$$Nu = 0.023\,\mathrm{Re}^{4/5}\,\mathrm{Pr}^{n} \tag{10.44}$$

where $n = 0.4$ for heating ($T_s > T_m$) and 0.3 for cooling ($T_s < T_m$).

$$Nu = 0.027\,\mathrm{Re}^{4/5}\,\mathrm{Pr}^{1/3}\left(\frac{\mu}{\mu_s}\right) \tag{10.45}$$

It is important to realize that most turbulent-based heat-transfer correlations are intrinsically empirical in nature and therefore are only applicable for very specific sets of conditions. For example, different correlations must be used under the same flow conditions, depending on whether there is heating or cooling of the flow, what the temperature difference between the wall and fluid is, and most important of all, what the level of turbulence is as characterized by the Re.

10.3 Two-Phase Convection in Microchannels

Two-phase flow cooling provides significant advantages over single-phase cooling in terms of heat-transfer rates and lower cooling temperatures. By taking advantage of the latent heat of phase change, boiling in microchannels can significantly increase the amount of heat removed from electronic components while sustaining a lower temperature, namely the saturation temperature. Two-phase flow boiling provides an enticing approach to achieve high heat-flux transfer rates on the order of 1 kW/cm^2.

Despite the potential heat-transfer benefits associated with two-phase flow cooling, several practical difficulties have prevented its use in actual microscale heat exchangers. Most of these difficulties are associated with the unstable nature of microchannel flow boiling at these scales.

10.3.1 Boiling Instabilities

Locally, some of the most stable boiling regimes present in macroscale flow are nonexistent in microscale flows. Namely, the incipient bubble boiling regime very common in macroscale duct flow is not possible in microchannel boiling. The small microchannel dimensions preclude the existence of multiple individual bubbles within the actual bulk flow. The same can be said for other macroscale flow boiling

regimes, such as churn flow. Instead, the number of microscale flow boiling regimes is very limited with the formation of bubbles leading almost instantaneously to an elongated vapor plug and thin, annular film regime. Formation of independent bubbles within the bulk flow is possible but only under very low heat loads and high-volume flow regimes, where the potential advantages of flow phase change are not fully exploited. The inherent nature of these flow regimes leads to very unstable behavior with the microchannel flow transition changing stochastically from single-phase liquid flow to metastable thin, annular liquid flow and, ultimately, to burnout and dryout conditions in which the flow has essentially transitioned to a single-phase vapor flow with low convective heat-transfer capabilities.

This local flow-instability behavior can propagate into a global instability behavior, with large pressure fluctuations and almost instantaneous microchannel flow transitions in multichannel heat-exchanger systems. Qu and Mudawar [22] reported on boiling flow instabilities arising in parallel mini- and microchannels arrangements and previously reported by Kandlikar et al. [23] and Hetstroni et al. [24], classifying them into severe pressure-drop oscillations and mild parallel-channel instabilities. They concluded that severe pressure-drop oscillation was the result of interaction between the vapor generation in the microchannels and the compressible volume in flow loop upstream of the heat sink. The parallel-channel instability only produced mild pressure fluctuations and was the result of density wave oscillation within each channel and feedback interaction between channels.

Peles et al. [25] developed and used a simplified, one-dimensional model of flow with a flat evaporation front dividing the liquid and vapor phases, along with experiments conducted on 16 mm–long, parallel triangular microchannels ranging in size from 50 to 200 μm to study the behavior of boiling two-phase flow in microchannel heat sinks. They concluded that the evaporating mechanism in two-phase flow in microchannels was considerably different from that observed in their macroscale counterparts. As stated previously, they observed that the most prevalent and characteristic flow regime in microchannels consisted of two distinct phase domains, one for the liquid and another for the vapor. A very short (on the order of the hydraulic diameter) section of two-phase mixture existed between the two. As such, they argued, the outlet vapor mass quality for a steady-state flow could only take on the values of zero (single-phase liquid flow) or unity (saturated or supersaturated vapor). Since the energy required for an outlet of quality zero is much larger than that for an outlet of quality one, an energy gap exists between those two levels, for which steady, evaporating two-phase flow is precluded in these microscale systems.

Peles et al.'s [25] approach looks at the instability problem from an energy barrier perspective. The heat-flux input is the driving force that can take the system from one state to the other and over the energy hump. Heat fluxes that bestow the system with energy levels in the gap region lead to instability. This is somewhat in contrast to the approach by Qu and Mudawar [22], who focus on the resistive-capacitive behavior of the upstream loop section as the key parameter for instability. The two approaches are complementary since it is the interaction between the vapor generation and the fluidic system characteristics that leads to the oscillations. The heat flux drives the evaporation fronts in both directions, therefore increasing the backward pressure of the system. The backward pressure leads to an increase in the pressure in the upstream loop section, which then feeds back into the

microchannel section and leads to a forward pressure push that can lead to expulsion of the evaporating front. Since the heat flux remains fixed at the gap energy level, the expulsion of the evaporating front leads to an unstable condition.

Xu et al. [26] studied parallel multichannel instability in a heat sink consisting of 26 rectangular microchannels 300 μm in width and 800 μm in depth. They found that the onset of flow instability (OFI) occurred under an outlet temperature ranging between 93°C and 96°C, several degrees below the saturation temperature of 100°C corresponding to the exit pressure conditions. They also identified three types of oscillations: large-amplitude/long-period oscillations (LALPOs), small-amplitude/short-period oscillations (SASPOs), and thermal oscillations (TOs). Chang and Pan [27] also conducted work on two-phase flow instability in a microchannel heat sink consisting of 15 parallel microchannels of rectangular cross section 100 μm in width and 70 μm in depth. They identified two different two-phase flow patterns under stable or unstable conditions. For the stable two-phase flow oscillations, bubble nucleation, slug flow, and annular flow appeared sequentially in the flow direction (Figure 10.3). For the unstable case, forward or reversed slug or annular flows appeared alternatively in every channel. Intermittent reversed flow of the two-phase mixture to the inlet chamber was observed (Figure 10.4). They also found that the pressure-drop oscillations could be used as an index of the appearance of reversed flow. Pressure fluctuations above 6 kPa would lead to flow instability with reversed flow to the inlet chamber.

Despite their similarities, single-microchannel and parallel-multimicrochannel instabilities are inherently different in nature. Single-microchannel instabilities arise primarily due to interactions between pressure fluctuations in the upstream flow delivery systems and the rapid and explosive nature of the phase change during boiling in the microchannel. This resistive-capacitive oscillation is also known as a Ledinegg instability. One way to suppress the onset and lessen the fluctuations of Ledinegg instabilities is to increase the flow resistance upstream of the heat sink, thereby reducing the upstream propagation of the backpressure effects from the sudden vapor generation in the microchannels. On the other hand, parallel-microchannel**<AQ: multimicrochannel?>** instability is primarily characterized by a rapid and random (in appearance) redistribution of the flow among the different microchannels. This flow redistribution is the result of the uniform pressure condition across the microchannels, along with the increase in the flow resistance in those microchannels undergoing boiling: flow increases in the low-resistance microchannels, while at the same time it decreases in the high-resistance ones (boiling microchannels) in order to maintain pressure equalization among them.

10.3.2 Pressure Drop and Heat-Transfer Coefficient

The two key parameters in the design of conventional convective-based cooling systems are the pressure drop and the convective heat-transfer coefficient. The same holds true for microchannel heat sinks. The pressure drop is one of the inputs (the other being volume flow rate) needed to assess the pumping-power requirements of the cooling system. Likewise, the convective heat-transfer coefficient provides a measurement of the cooling effectiveness of the system.

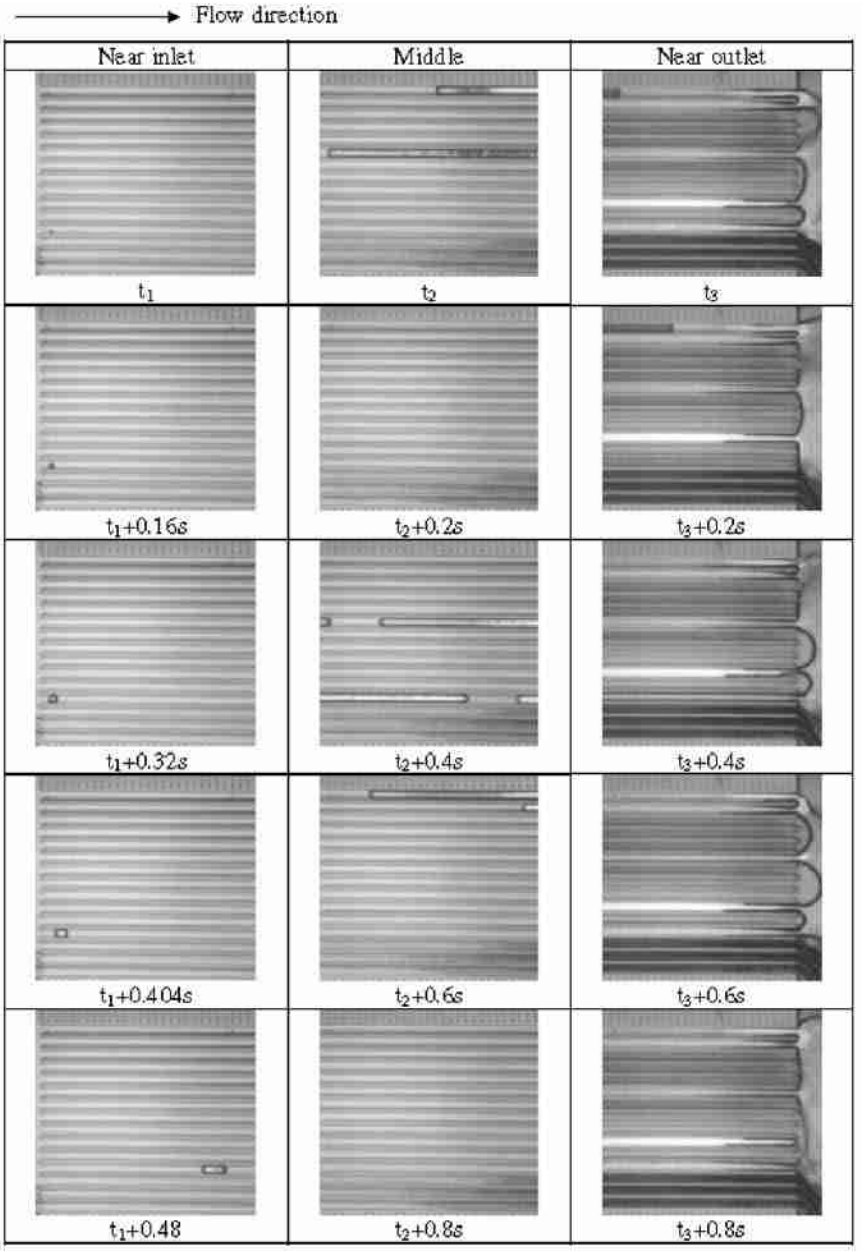

Figure 10.3 Evolution of two-phase flow patterns in the entrance, middle, and exit regions of a heat sink consisting of 15 parallel microchannels of rectangular cross section 100 μm in width and 70 μm in depth. In this stable two-phase flow, oscillations, bubble nucleation, slug flow, and annular flow appear sequentially in the flow direction [27].

The characteristics of pressure drop in microchannel two-phase flows are very peculiar. In addition to the frictional component, two-phase-flow pressure drop is characterized by the presence of the acceleration component. As the liquid phase changes into vapor, there is a sudden decrease in fluid density accompanied by an increase in fluid volume. In order to maintain the prescribed mass flow rate, the lighter fluid must be accelerated, leading to an increase in pressure drop: additional

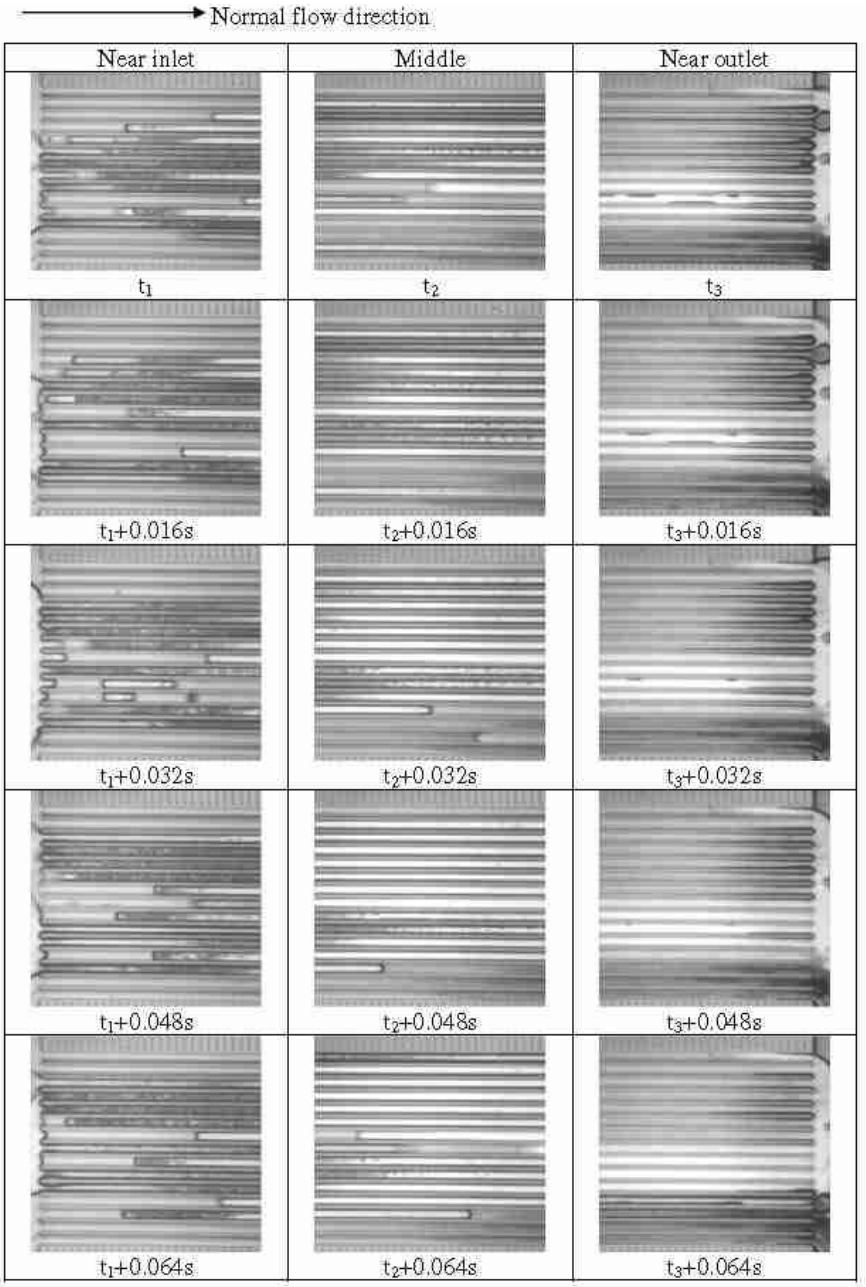

Figure 10.4 Evolution of two-phase flow patterns in the entrance, middle, and exit regions of a heat sink consisting of 15 parallel microchannels of rectangular cross section 100 μm in width and 70 μm in depth. In this unstable case, forward or reversed slug or annular flows appear alternatively in every channel. Intermittent reversed flow of the two-phase mixture to the inlet chamber is also observed [27].

work must be done in order to accelerate the vapor to the required velocity. It is interesting to note that due to the higher kinematic viscosity of vapor as compared to liquid water, for a particular mass flow rate, the required pressure drop for vapor is higher than that for liquid water. Although this seems to fly in the face of or to con-

tradict the stated lower-mass flow rates required for microchannel boiling cooling systems, it must be recalled that the benefits of boiling two-phase flow are associated with the latent heat of phase change and not with the use of single-phase vapor as the coolant.

Several studies exist on the topic of pressure drop in two-phase flows in microchannels. Most of them are experimental in nature and focus on the establishment of relationships between flow regime and pressure drop. They generally revolve around the use of an experimental sample retrofitted for optical access. Pressure-drop measurements between inlet and outlet are supplemented by white-light visualization studies of the different flow structures.

Koo et al. [28] highlighted the importance of pressure drop in the performance of microchannel heat sinks. It is demonstrated in this study how the wall-temperature distribution is governed in part by the coupling between the pressure drop and the saturation temperature and how it influences the overall performance of the microchannel heat sink. Employing a homogeneous two-phase flow model developed in an earlier work [10, 29], they investigated the effect that a one-dimensionally varying heat flux had on the temperature field. They found that the most advantageous configuration was to apply most of the heat to the latter part of the two-phase microchannel heat sink. Under this spatial arrangement, the temperature increases in the liquid phase region due to sensible heating are minimized by limiting the heat input in this upstream section. Lower temperature management is also achieved by placing the high-heat-input section downstream, where flow boiling occurs. In this two-phase region, fluid temperature is limited to the saturation value by the latent heat. As the flow pressure decreases in this section as it approaches the exit value, so does the fluid saturation temperature and, hence, the wall temperature. Interestingly enough, under this arrangement, the highest wall temperature is not located at the higher heat-flux region but rather near the inlet, which is the lower heat-flux region. Based on these results, Koo et al. [28] concluded that the pressure drop is the most critical factor in the design of microchannel heat sinks and that careful optimization should be performed in order to minimize pressure drop along the microchannels (higher pressures translate into higher saturation temperatures).

The number of heat-transfer studies is less prevalent, probably due in part to the difficulties associated with accurately measuring the heat-transfer coefficient. Properly measuring the convective heat-transfer coefficient requires knowledge of the heat transferred to the fluid in addition to the surface and bulk fluid temperatures. Measurement of the actual amount of heat transferred to the fluid is a difficult task. In most cases, a resistive heater is used as the heat source, and the total heat generation can be calculated from the joule heating equation. However, not all of the heat is convected by the microchannel flow, and environmental loses need to be accounted for. These include primarily heat losses by natural convection to the environment. Measuring the local wall and bulk-flow temperature is also an extremely difficult task. Local wall-temperature measurements can be achieved through the use of temperature sensors, such as microthermocouples or integrated resistor temperature detectors (RTDs), which can be incorporated into the fabrication of the test samples, such as those developed and employed by Zhang et al. [10]. RTDs rely on the dependence of resistivity on temperature. Zhang et al. [10] used

microfabricated beam suspended silicon microchannels to investigate two-phase flow boiling behavior under constant heat-flux boundary conditions. RTDs and heaters were incorporated into the back side of the silicon beam by ion implantation, allowing for distributed temperature measurements and heating (Figure 10.5). By using deep reactive ion etching (DRIE), rectangular microchannels with hydraulic diameters in the range of 25 to 60 μm were fabricated on a suspended silicon bridge reducing the channel wall thickness and effectively preventing conduction heat losses. Both homogeneous and separated (annular) flow models were developed and validated against pressure and temperature measurements carried out in the microchannels sample. Measuring the local bulk-flow temperature is extremely difficult. Optical techniques such as fluorescence can be used for these purposes, but even in this case, measurements are normally qualitative at best. Under very specific instances and for very specific flow regimes, the convective heat-transfer coefficient can be inferred from the morphology of the flow structure. This is the case for the stratified and annular flow regimes, for which the convective heat-transfer coefficient can be determined from the thickness of the liquid film surrounding the heated wall. For this particular flow regime, the convective heat-transfer coefficient can be calculated from the following simple expression [30]:

$$h = \frac{k_f}{\delta} \tag{10.46}$$

The convective heat-transfer coefficient in two-phase flow is a very dynamic, if not outright unstable, quantity due to the unsteady nature of this type of flow. As can be seen from (10.46), the thinner the film thickness is, the higher the heat-transfer coefficient. However, thin liquid-film thickness can quickly lead to burnout or dryout, where the liquid film has completely disappeared, leaving only a vapor core filling the microchannel. Under these conditions, the flow has become single phase again, but with a much lower conductivity, namely, that of the vapor.

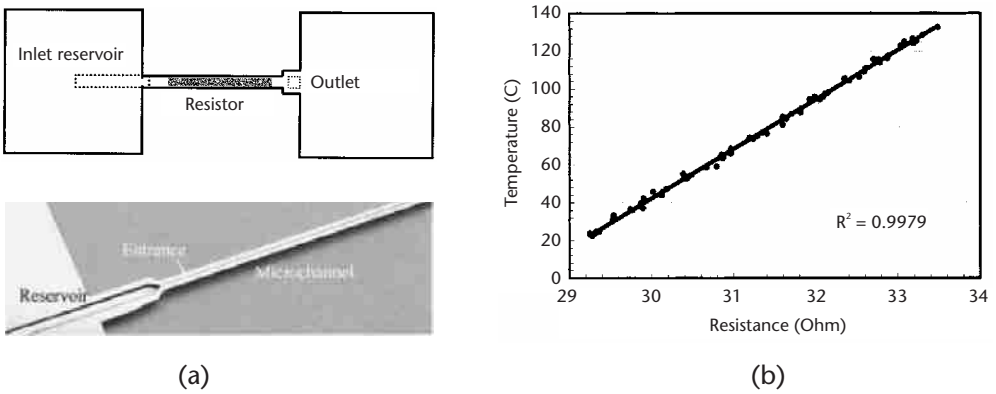

Figure 10.5 (a) Microfabricated beam suspended silicon microchannels are used to investigate two-phase flow boiling behavior under constant heat-flux boundary conditions. Resistance temperature detectors (RTDs) and heaters were incorporated in the back side of the silicon beam by ion implantation, allowing for distributed temperature measurements and heating. (b) An RTD calibration curve shows the linear dependence between resistance and temperature [10].

10.4 Modeling

Unlike single-phase flow cooling, where macroscale correlations and models are still applicable, microchannel two-phase flow cooling requires the development of very specialized and specific models. The wealth of two-phase and boiling flow models available for macroscale systems have very limited applicability in microchannel systems. Surface tension has drastically different effects in microscale two-phase flow relative to its macroscale counterpart. Although surface tension is relevant in macroscale two-phase flow due to its influence in flow-transition criteria and bubble nucleation dimensions, its impact in microscale two-phase flow is significantly different and arguably more important. In microchannel two-phase flow, the characteristic bubble nucleation dimensions are comparable to the hydraulic diameter, leading to a cross section expansion confinement that abruptly redirects bubble growth to the axial direction. Capturing these confinement interactions is fundamental to the development of microscale boiling and phase-change flow models. Likewise, the gravitational effects included in macroscale models become almost irrelevant in microscale models. Determining whether these effects should be included in a particular model is important because it can greatly reduce the amount of computational complexity, allowing for better usage of the computational budget toward more relevant phenomena.

The two basic approaches to two-phase modeling are homogeneous flow modeling and separate flow modeling. As their names imply, homogeneous flow modeling assumes that the two phases intermix in a homogeneous configuration with identical properties. In a separate flow model, each phase is treated individually, while accounting for interactions between the two. Intermediate approaches can be considered a hybrid configuration of the two, but a clear distinction can be made in terms of the number of fundamental conservation equations used. Single mass, momentum, and energy equations are usually the norm in homogeneous flow models. Any implementation of more than one conservation equation for any of the three fundamental quantities of interest should be considered a separated flow model.

10.4.1 Homogeneous Flow Modeling

Homogeneous flow models rely on the assumption that flow behavior can be modeled by assuming that the bulk flow consists of a homogeneous intermix of the phases involved with equal property values between the two phases. Fundamentally, the velocity and temperature between the phases is considered the same. The homogeneous flow properties are normally characterized by the volume or mass average of the "coflowing" phases.

Homogeneous flow models have advantages in term of simplicity and are quite accurate in flows that are inherently "well" mixed or exhibit dispersed characteristics of one phase into the other, such as macroscale bubbly flows. However, it has been shown that they can also be applied to microscale two-phase flows, despite their inherent nonhomogeneous nature.

Homogeneous flow models can be successfully implemented in flows that are inherently nonhomogeneous by introducing constitutive equations that take into

account the interactions between the two phases [31]. Despite the use of single-phase conservation equations, these flows are sometimes considered a type of separated flow model.

Koo et al. [29, 32] used a homogeneous flow model that employed the correlation of Kandlikar [33] for heat-transfer-coefficient calculations to simulate and compare the performance between a conventional heat sink and a parallel array of 18 microchannels for a 3-D IC consisting of two functional silicon layers. The model was based on a two-phase flow regime consisting of a homogeneous core composed of a mist of liquid droplets and vapor moving at the same velocity, surrounded by a very thin, slow-moving liquid film (Figure 10.6). Central to the homogeneous model treatment is the assumption of identical velocities for the liquid and vapor phases in the core, along with neglect of the slower velocity in the thin surrounding film, treating it simply as a solid boundary with lower conductivity than the microchannel wall. Several nonuniform power distribution conditions were simulated by using different layouts of the logic and memory regions. It was found that a two-phase microchannel network outperforms current conventional heat sink cooling technology in terms of both junction temperature uniformity within each layer and temperature difference between the two layers.

Despite the success of two-phase homogeneous flow models in predicting flow behavior in microchannels, their applicability is somewhat limited. As we have seen from the previous examples, homogeneous flow models can be successfully applied to microchannel flows in which one of the phases is dominant or the two-phases flow at the same velocity. However, under highly nonuniform flow conditions, such as is the case with the bubble/slug flow regime, only separated flow models can capture the relevant physics of the flow.

10.4.2 Separated Flow Modeling

Separated flow models on the other hand, although more accurate, tend to be too computationally expensive, making them hard to implement on large systems. They are characterized by the use of independent conservation equations for each of the

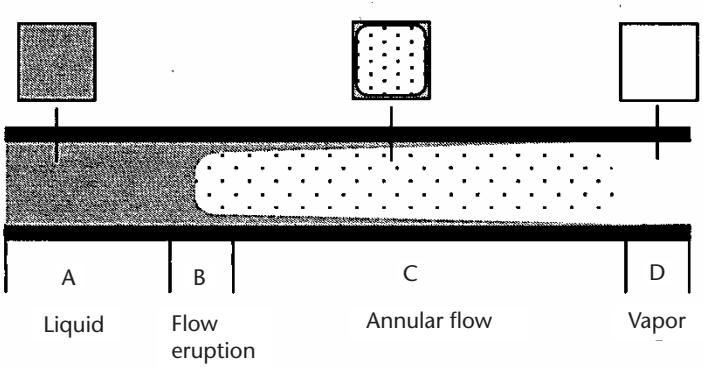

Figure 10.6 Two-phase flow regime used in the development of the homogeneous flow model by Koo et al. [29]. The flow structure consists of a homogeneous core composed of a mist of liquid droplets and vapor moving at the same velocity, surrounded by a very thin, slow-moving liquid film.

phases. At the far end of the separated flow modeling spectrum, the phases are treated as completely distinct entities, allowing for exchanges between them and using a computational approach that keeps track of interface locations as well as properties for each of the phases. This sort of approach is extremely computationally intensive and almost impossible to implement in large-scale systems. Numerical simulations of this type are primarily used to study flow behavior locally.

By relaxing the interface tracking requirements and limiting the amount of interaction between the phases, separated flow models can take on simpler forms that are much easier to handle computationally, while retaining the key benefits associated with treating each phase independently.

The simplest form of separated flow models treats the two phases completely separately, restricting any type of interface exchange. In this type of model, the interaction between the phases is included through constitutive equations that are dependent on the relative velocity difference between the phases. Some specific examples include the Lockhart-Martinelli model for pressure-drop predictions in two-phase flows [34]. The key velocity-differential constitutive correlations in the Lockhart-Martinelli model are empirical in nature and rely on flow-regime maps for their proper implementation. Another example is the particle trajectory model, which is used in dispersed flows (i.e., one phase in the form of "particles" and the other phase as continuous) [35]. Despite the Lagrangian nature of this model, it is a simplified separate flow model because there is no tracking of the actual interfaces; rather, the particles are treated as "points" with relevant characteristics and forces acting upon them. One final example of this type of model is the drift-flux model, which has a very similar conception as the Lockhart-Martinelli model but with stronger coupling between the relative motions (velocity difference) of the phases. The drift-flux model can appropriately handle countercurrent flow and is thus particularly useful in dealing with the limitations of other models in this respect.

The next level of complexity in separated flow models is referred to as two-fluid models. These models treat each phase separately and do not keep track of interface locations, but they do allow for interface exchanges between the different conservation equations. The heart of these models is in the constitutive equations and relations used to model interface exchanges.

Finally, there are separated flow models that completely account for each phase and their interactions through interface tracking. These models are confined to the realm of computational fluid dynamics (CFD) codes and algorithms and, due to their computational complexity, are restricted to the study of local two-phase flow phenomena. Interface tracking is achieved through different methodologies, such as the volume-of-fluid (VOF) approach, where the void fraction of the computational cells is used as the parameter dictating interface location: value of one for an all-gas phase cell, value of zero for an all-liquid phase cell, and any other value in between for an interface cell (subcell interface location is computed through piecewise linearization with adjacent cells and void-fraction value). Implementing a model of this type on a global system of large scale is extremely impractical, if not outright impossible.

Garimella et al. [36] developed an experimentally validated, separated two-phase flow model for pressure drop during intermittent flow of condensing

refrigerant R134a in horizontal microchannels. The model was based on the observed slug/bubble flow regime and the assumptions about the shape of the bubble, film, and slug regions proposed by Suo and Griffith [37] and Fukano et al. [38]. The slug/bubble flow regime is considered periodic, and a unit cell consists of a cylindrical bubble surrounded by a uniform annular film of liquid. The bubble/annular film section is bounded by liquid slugs on either side, with the bubble moving faster than the slugs (Figure 10.7). The liquid velocity in the annular film is much slower than both the bubble and slug velocities. The total pressure drop is calculated as the sum of the purely frictional pressure drops from the slug and bubble/film regions and the losses associated with the flow between the film and the slug. They found that the pressure drop for the same ratio of tube length to hydraulic diameter, L_{tube}/D_h, **<AQ: edit okay?>**increases almost linearly with increasing quality and more sharply with decreasing tube diameter and increasing mass flux.

10.5 Pumping Considerations

Overcoming the large pressure drops associated with microchannel cooling in an efficient manner is one the major roadblocks to successful implementation of this technology. In order to realize the potential cooling performance of this promising technology, pumps capable of sustaining large pressure drops and flow rates are required. This necessitates the use of large pumps with substantial power requirements. This diminishes the size benefits of using microchannels for cooling, while the imposed taxing on the power greatly reduces the overall efficiency and heat-enhancement benefits of the technology. It also has negative implications in terms of noise issues. Thus, there is a great interest in finding a micropump technology capable of delivering the required performance needed to achieve the full potential of this technology. Although several potential candidates exist, there are no clear favorites, and, overall, none of the existent micropumps is capable of delivering the pressure and flow rates needed.

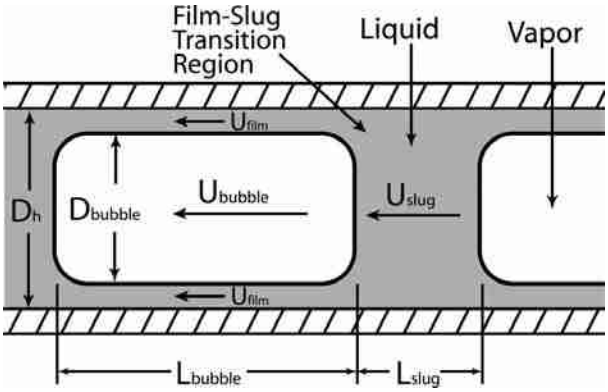

Figure 10.7 Two-phase flow regime used in the development of the separated flow model by Garimella et al. [36]. The slug/bubble flow regime is considered periodic, and a unit cell consists of a cylindrical bubble surrounded by a uniform annular film of liquid. The bubble/annular film section is bounded by liquid slugs on either side, with the bubble moving faster than the slugs.

Before reviewing the existing technologies, it is important to develop a reference framework on which the necessary pressure-drop and flow-rate requirements are based. Here, we review and present the first-order analysis performed by Singhal et al. [39, 40], which provides a good starting point. The analysis is based on the minimum pressure head and flow rate required under specific thermal constraints, namely, the maximum temperature at any point in the chip and the maximum-temperature gradient on the chip that can be tolerated.

Assuming fully developed velocity and temperature flow conditions under a constant heat-flux boundary condition, the temperature profiles of both the mixed mean bulk-flow temperature and the surface temperature are both linear. Under these conditions, it can be shown that the required liquid flow rate needed to sustain a given temperature gradient is given by

$$Q = \frac{q}{\rho c_p L_d (dT / dx)} \tag{10.47}$$

such that, for a given maximum allowable temperature gradient,

$$Q \geq \frac{q}{\rho c_p L_d (dT / dx)_{\max}} \tag{10.48}$$

Likewise, the required flow rate for a given maximum allowable temperature can be calculated using (10.34), (10.48), and Newton's law of cooling, (10.28), as well as from the notion that the maximum fluid and chip temperatures occur at the exit. Thus, we have

$$Q \geq \left(\frac{q}{\rho c_p}\right) \frac{1}{\left[T_{\max} = T_{f,i} - \dfrac{q(w_c + w_w)}{NukL_d W_d} \dfrac{\alpha}{(1+\alpha)^2}\right]} \tag{10.49}$$

Given that the flow rate and pressure drop are related through (10.3) and (10.13), the pressure-drop requirements can also be specified:

$$\Delta p \geq \left(\frac{q\mu}{8\rho c_p W_d (dT / dx)_{\max}}\right) \frac{(1+\alpha)^2}{\alpha^3} f \operatorname{Re} \frac{w_c + w_w}{w_c^4} \tag{10.50}$$

and

$$\Delta p \geq \left(\frac{q\mu L_d}{8\rho c_p W_d}\right) \frac{\dfrac{(1+\alpha)^2}{\alpha^3} f \operatorname{Re} \dfrac{w_c + w_w}{w_c^4}}{\left[T_{\max} - T_{f,i} - \dfrac{q(w_c + w_w)}{NukL_d W_d} \dfrac{\alpha}{(1+\alpha)^2}\right]} \tag{10.51}$$

depending on whether the maximum-temperature gradient or the maximum-temperature requirements are considered, respectively.

If the thickness of the microchannel walls (w_w) and aspect ratio (α) are assumed to be fixed, a valid constraint given microfabrication limitations, a pressure-drop versus flow-rate operating map can be constructed by plotting (10.48) against (10.50) and (10.49) against (10.51) for a given heat load (q) as functions of microchannel width (w_c). We can start with the maximum-temperature constraint. Plotting (10.49) against (10.51) for a given heat load and as a function of microchannel width, we get the dot-dashed line in Figure 10.8. All the points to the right of and above this line are within the "operating region," where the maximum-temperature constraint is satisfied. We will now consider the maximum-temperature-gradient constraint. Looking at (10.48), it is apparent that the required flow rate for a given temperature-gradient constraint is independent of microchannel width and only a function of the temperature gradient. However, the pressure drop, as given by (10.50), does depend on the microchannel width, and it decreases as the microchannel width increases. Thus, the "operating region" boundary line is defined by a vertical line crossing the flow-rate axis at the required value needed to satisfy the maximum-temperature-gradient constraint. All the points to the right of this line and above the minimum required pressure drop compose the "operating region" for a given temperature-gradient ceiling. As depicted in Figure 10.8, the intersection of these two regions comprises the global "operating region" of the microchannel heat sink for a set of given thermal constraints.

The suitability of a given pump for a particular microchannel heat sink design is assessed by superimposing the pump curve and corresponding pressure-head versus flow-rate load characteristics of the microchannel heat sink on top of the "operating region" map. The pump curve refers to the flow-rate versus pressure-head operating characteristics of the pump and is usually obtained experimentally. In general, the pressure head than can be sustained by the pump decreases as the flow rate increases. The pressure-head versus flow-rate load characteristics of the heat sink are obtained by using (10.3) or (10.13). The intersection of the pump curve and the heat sink load curve determine the "operating point" of the overall cooling system. Whether this point lies within the "operating region" determines the suitability of

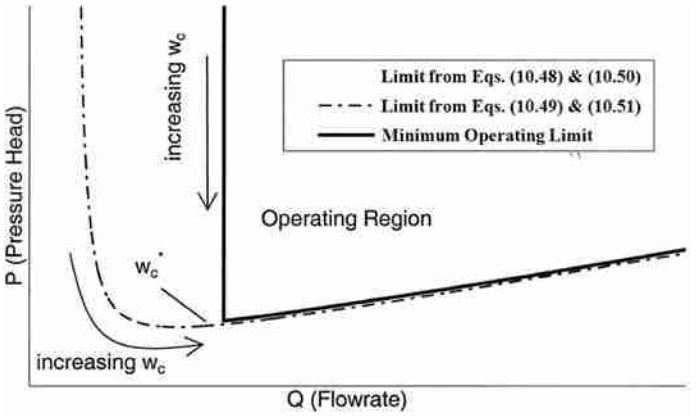

Figure 10.8 "Operating region" of a microchannel heat sink for a set of given thermal constraints. This map is constructed by plotting and combining the pressure-flow requirements, given maximum-temperature-gradient and maximum-temperature constraints for the microchannel heat sink [39, 40].

the system as a whole for achieving the desired thermal conditions. This is depicted in Figure 10.9, in which the open dots represent "operating points" of pump–heat sink combinations capable of dissipating the required heat to maintain suitable thermal operating conditions on the chip. On the other hand, the solid dots represent "operating points" for pump–heat sink combinations that would not meet the required thermal constraints.

The previous analysis is also useful as a tool for heat sink optimization. The apex of the "operating region" demarcation line represents the minimum pumping requirements in terms of both pressure head and volume flow rate capable of achieving the desired thermal conditions. The microchannel width corresponding to this point represents an optimal value for this parameter, given the fixed constraints on the microchannel wall with **<AQ: text missing here?>** and aspect ratio. This optimal microchannel width can be obtained by equating the flow rates from (10.48) and (10.49):

$$w_c^* = \frac{NuL_d W_d}{q}\left(T_{\max} - T_{f,i} - L_d\,(dT/dx)_{\max}\right)\frac{(1+\alpha)^2}{\alpha} - w_w \tag{10.52}$$

Singhal et al. [39, 40] presented an illustrative example to assess the suitability of current miniature conventional pumps as well as several vanguard technology micropumps. The example is based on the use of water as the cooling liquid; the other inputs used in the example are presented in Table 10.1. The results of the exercise are summarized in Figure 10.10, which overlays the thermal-constraints "operating region" map, along with the load curves for two specific microchannel heat sinks (100 and 400 μm microchannel width) in the range considered ($50 \leq w_c \leq 800$), against the pump curves for conventional centrifugal, gear, and flexible-impeller miniature pumps, as well as the curves for several micropumps,

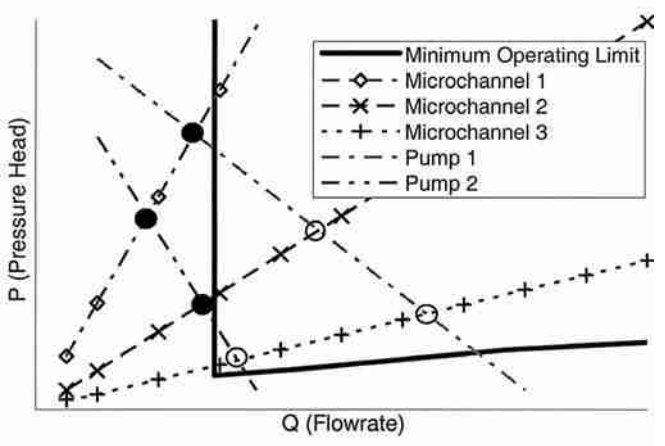

Figure 10.9 Overlay of thermal-constraints "operating region" for a microchannel heat sink of fixed aspect ratio, hypothetical pump curves, and corresponding pressure-head versus flow-rate load characteristics for the heat sink for different microchannel widths. The intersection of the pump curve and the heat sink load curve determine the "operating point" of the overall cooling system. Whether this point lies within the operating region determines the suitability of the system as a whole for achieving the desired thermal conditions. The open dots represent suitable pump–heat sink combinations, while the opposite holds for the solid dots [39, 40].

Table 10.1 Inputs Used in the Pump Suitability Example by Singhal et al. [39, 40].

Parameter	*Value*
Coolant	
Density, ρ	984.25 kg/m^3
Specific heat, c_p	4184 J/kgK
Viscosity, μ	4.89 × 10–4<AQ: 10^{-4}?> N·s<AQ: N•s for Newton second?>/m^2
Chip	
Length, L	1 cm
Width, W	1 cm
Microchannels	
Aspect ratio, μ	6
Channel width, w_c	50 to 800 μm
Wall thickness, w_w	100 μm
Thermal Parameters	
Heat load, q	100 W
Maximum chip temperature, T_{max}	80°C
Maximum chip-temperature gradient, $(dT/dx)_{max}$	5°C/cm

namely, a valveless (nozzle-diffuser) micropump using piezoelectric actuation, an injection-type electrohydrodynamic (EHD) micropump, an electroosmotic micropump, a rotary micropump, and a piezoelectric micropump. None of the micropumps presented in the literature can meet the thermal and load requirements of the microchannel heat sinks as stand-alone units, especially in terms of volume flow rate. Therefore, the pump curves depicted in Figure 10.10 represent parallel arrangements of several micropumps capable of achieving the required volume flow rates. The conventional pumps and parallel micropump arrangements are also compared in Table 10.2 in terms of maximum volume flow rate, maximum pressure head, and size. For the micropumps, the size of the individual micropumps is presented along with the number of micropumps in parallel needed to achieve the required volume flow rate (number in parentheses). Although the volume flow rate and pressure head provided by the conventional pumps are much larger than those provided by the micropump combinations, the opposite is true in terms of the size metric.

Table 10.2 Comparison of the Capabilities and Sizes of the Different Pumps Considered by Singhal et al. [39, 40]

Pump	*Maximum Flow Rate (L/min)*	*Maximum Pressure (kPa)*	*Size (mm^3)*
Miniature centrifugal magnetic drive pump	11.36	344.74	114.3 × 95.2 × 82.5
Miniature gear pump 1	1.5	144.79	101.6 × 44.5 × 66.7
Miniature gear pump 2	2.3	68.95	87.4 × 81.0 × 92.1
Flexible-impeller pump	14.38	68.95	152.4 × 114.3 × 107.9
Valveless micropump	0.345	74.53	15 × 17 × 1.4 (150x)
Injection-type EHD micropump	0.35	2.48	3 × 3 × 0.76 (25x)
Electroosmotic micropump	0.32	202.65	10 × 10 × 15 (400x)
Rotary micropump	0.35	1.4	3.17 × 3.17 ×0.6 (1,000x)
Piezoelectric micropump	0.375	1.7	5.3 × 5.3 × 1.5 (250x)

From Figure 10.10, it is apparent that, for the microchannels of width 100 μm only, the conventional pumps and the electroosmotic and the valveless micropump combinations satisfy the pumping requirements of the microchannel heat sink design. For the heat sink with microchannel width of 400 μm, all the conventional pumps, as well as micropump combinations, provide the desired pumping requirements to satisfy the thermal constraints. Thus, from the previous analysis of Singhal et al. [39, 40], it is apparent that electroosmotic and valveless micropumps are the only feasible microscale technologies that would provide comparable pumping capabilities to their conventional counterparts, while maintaining their edge in terms of overall size advantage. However, the feasibility of these two micropump technologies is marginal at best, even with the relatively low heat load of 100 W/cm^2 used in this example. Projected future heat loads, and even existing ones in the microelectronics industry, exceed this value, making the current state of the art of these technologies unsuitable for the task, particularly in 3-D IC architectures. Further research and development in micropump technologies is needed to achieve the pumping characteristics that would make them a realistic feasibility for current and future IC designs.

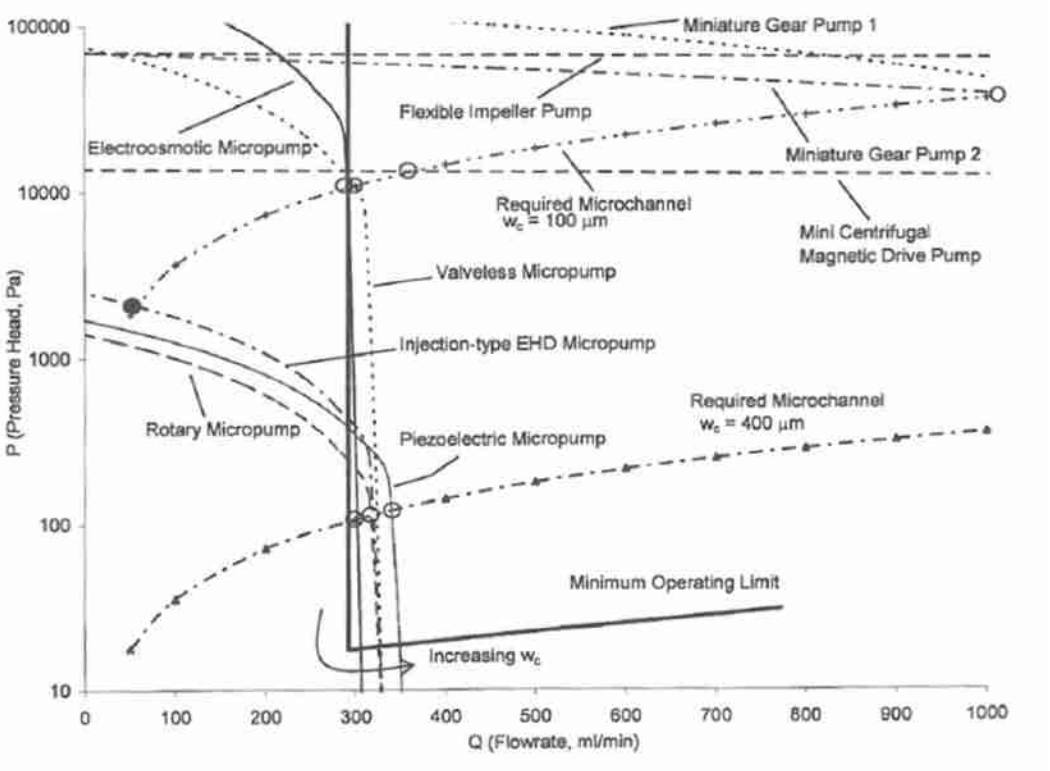

Figure 10.10 Overlay of the thermal-constraints "operating region" map, along with the load curves for two specific microchannel heat sinks (100 and 400 μm microchannel width) in the range considered (50 = wc = 800) by Singhal et al. [39, 40], against the pump curves for conventional centrifugal, gear, and flexible-impeller miniature pumps, as well as the curves for several micropumps, namely, a valveless (nozzle-diffuser) micropump using piezoelectric actuation, an injection-type electrohydrodynamic (EHD) micropump, an electroosmotic micropump, a rotary micropump, and a piezoelectric micropump.

10.6 Optimal Architectures and 3-D IC Considerations

The proper design of successful microchannel heat sinks is a typical example of an engineering trade-off. The small dimensions involved allow for higher heat-transfer rates due to the inherent shorter diffusion lengths and higher fluid velocities, which translate into large convective heat-transfer coefficients and lower thermal resistances in general. On the other hand, the use of microchannels introduces a challenge in terms of the pressure drops required to maintain the desired flow rates. Therefore, it is important to optimize the microchannel geometry and heat sink architecture in general so that the improvements in thermal performance overcompensate for the increased burden on pumping-power requirements.

Despite their proven cooling benefits, conventional parallel straight microchannel heat sinks have inherent drawbacks in terms of temperature uniformity and required pressure drops. Serpentine microchannel arrays can lead to better temperature uniformity, but they exacerbate the negative trend toward larger pressure drops due to increased channel lengths. These issues are compounded in 3-D IC architectures, in which the use of single straight microchannels would make it impossible to achieve any reasonable degree of temperature uniformity and would incur extremely high pressure drops in any attempt to compensate for this drawback through the use of a large coolant flow rate.

Different optimization schemes have been studied in an attempt to improve the thermal performance and lessen the pumping requirements of microchannel-based heat sinks for cooling planar architectures. Wei and Joshi [41, 42] studied the use of stacked 2-D microchannel heat sinks for cooling a single heat-generating device layer (Figure 10.11). They employed a simple 1-D resistance network to evaluate the overall thermal performance of a stacked microchannel heat sink. They found that under fixed pressure-drop or pumping-power constraints, multilayered

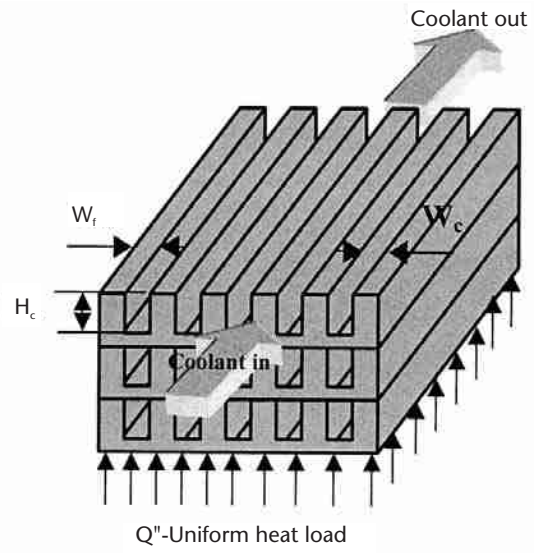

Figure 10.11 Schematic of a three-dimensional microchannel stack used in the optimization study of Wei and Joshi [41, 42].

microchannel heat sink performance is superior to that of a single-layered one. However, under fixed flow-rate constraints, optimal thermal performance is achieved for a two-layered microchannel heat sink system. The multilayered architecture acts as a heat spreader, increasing the overall surface area over which heat is transferred to the fluid, thereby reducing the overall thermal resistance of the system under fixed pressure-drop constraints. Although the overall thermal resistance is reduced when two layers are used instead of one for the case of fixed-volume flow-rate conditions, adding further layers tends to increase the overall thermal resistance. The addition of more channels results in lower flow rate and velocity in each channel, resulting in a decrease in heat-transfer coefficient, even though there is an increase in heat-transfer surface area. Under fixed pumping-power constraints, the increase in heat-transfer surface-area effect overcompensates for the reduction in channel flow velocity, leading again to an overall reduction in thermal resistance.

Koo et al. [32] furthered the study of stacked microchannel heat sinks by adding several heat-generating device layers sandwiched in between the microchannel layers. They looked at a 3-D IC with integrated microchannel cooling system consisting of three device layers and two microchannel layers arranged in an alternating pattern (Figure 10.12). In addition, they developed and implemented a two-phase flow model to account for boiling in the microchannels. Finally, they analyzed the effects of nonuniform power generation on the cooling of 3-D ICs by looking at a simplified architecture consisting of a single-microchannel cooling layer stacked between two device layers. They split the device into logic circuitry, accounting for 90% of the power generation, and memory, accounting for 10% of the total 3-D IC power generation. Four different stack schemes were analyzed (Figure 10.13). For case (a), the logic circuit occupied the whole of device layer 1, while the memory was on device layer 2. In the other cases, each layer was equally divided into memory and logic circuitry. For case (b), a high-heat-generation area was located near the inlet of the channels, while it was near the exit of channels for case (c). Case (d) had a combined thermal condition in which layer 1 had high heat flux, and layer 2 had low heat dissipation near the inlet. The total circuit area was 4 cm^2, while the total power generation was 150W. From their results, they concluded that the optimal configuration was to manage the higher power dissipation toward the microchannel heat sink outlet region since this would minimize the pressure drop of

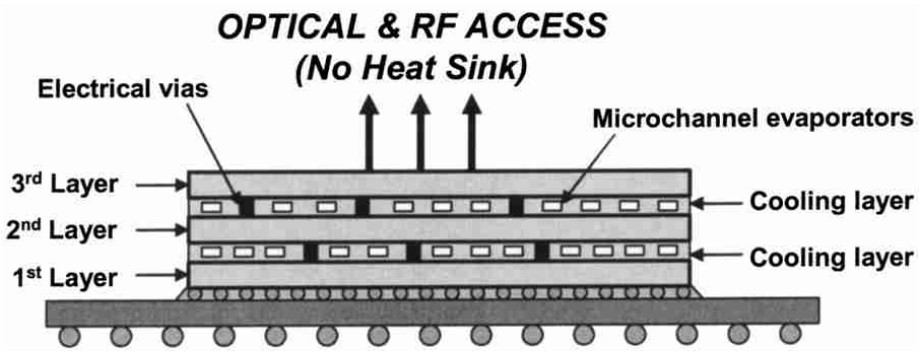

Figure 10.12 3-D IC with integrated microchannel cooling system consisting of three device layers and two microchannel layers arranged in an alternating pattern used in the study by Koo et al. [32].

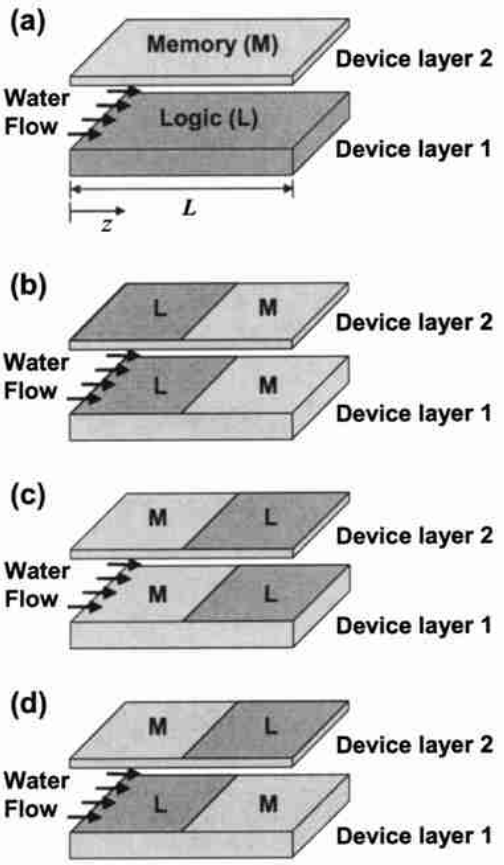

Figure 10.13 Two-layer 3-D circuit layouts for evaluating the performance of microchannel cooling. The areas occupied by memory and logic are the same, and the logic dissipates 90% of the total power consumption [32].

the two phase near the highest heat-flux regions, thereby decreasing the local wall temperature. They reasoned that if more heat is applied to the upstream region, boiling occurs earlier, resulting in increased pressure drop in the channel. Also, the average junction temperature was lower and the temperature field was more uniform employing this power-generation configuration.

Enhanced thermal and fluidic performance can also be attained by using manifold microchannel (MMC) heat sinks. Unlike traditional microchannel heat sinks, MMC heat sinks have several alternating inlet and outlet ports spanning the length of the parallel-microchannel arrangement, rather than a single inlet and outlet. Introducing multiple, equally spaced, alternating inlet-outlet arrangements effectively converts a long microchannel into a series of smaller microchannels. This has several effects. First, by reducing the overall length that fluid must traverse in the microchannel, pressure is reduced by a factor roughly equal to the number of manifold inlet-outlet pairs. Second, the bulk flow and convective resistances are both reduced, also consequences of the reduction in effective microchannel length. The bulk resistance arises as a consequence of the streamwise temperature increase in the bulk flow. The shorter distance traversed by the flow translates into lower bulk-temperature rise and therefore lower bulk resistance. The convective resistance

is inversely proportional to the convective heat-transfer coefficient. Breaking up the single-microchannel flow into multiple smaller microchannel flows translates into a larger number of developing entry regions, where the Nusselt number and, consequently, the convective heat-transfer coefficient are higher.

The MMC concept was first introduced by Harpole and Eninger in 1991 [43]. They developed a complete two-dimensional single-phase flow/thermal model of the concept and optimized its design parameters for the case of a 1 kW/cm^2 heat flux with a top surface temperature of 25°C. They analyzed MMCs having between 10 and 30 inlet-outlet manifold pairs per centimeter, found that the optimal value was 30, meaning that performance was always improved by adding extra manifold pairs, and concluded that their number should only be limited by manufacturing constraints. Through their design-parameter optimization, they were able to achieve effective heat-transfer coefficients on the order of 100 W/cm^{2}K with a total pressure drop of only 2 bar. Copeland [44] and Copeland et al. [45] have further analyzed MMC heat sink performance through analytical, experimental, and numerical studies. Of particular interest are the thermal results in [45], in which the authors employed a 3-D finite element model under isothermal wall conditions. They found that channel length or equivalent spacing between inlet and outlet for a manifold pair had almost no significant effect on thermal resistance, though the pressure drop was reduced considerably as this length was reduced.

Further improvements in terms of reduced pumping power and enhanced thermal performance of microchannel heat sinks can be achieved through the introduction of fractal and nonfractal tree-branching microchannel networks. Gosselin and Bejan [46] have demonstrated that tree-branching architectures can be used to optimize fluidic networks in terms of pumping-power requirement. Their findings can be summarized as follows: (1) pumping power is the appropriate cost function in the optimization of fluidic networks, not flow resistance or pressure drop, and minimization of each function leads to different ideal network architectures (in some special instances, pumping-power and pressure-drop optimization lead to the same solution); (2) minimum pumping-power networks do not exhibit loops; and, most importantly, (3) under pumping-power constraints, spanning networks (point centered outwards) containing branching points (Gilbert-Steiner points) provide the best architecture. The second and third points are the basis for the ideal tree-branching geometry. Bejan [47] also extends the concept of using fluidic tree networks for the optimization of volumetric cooling problems. Invoking again the minimization of pumping power as the appropriate parameter for system optimization, he derives a three-quarters power law relating heat dissipation to volume ($q = V^{3/4}$) as the optimal relationship between the two, given the pumping-power constraints. Pence [48] employs the bioinspired analogy of the circulatory system as an efficient transport system to argue for the use of multiscaled branching flow networks in cooling applications. She points out that it would be inefficient for the heart to pump blood entirely through capillaries originating from the heart (source) and ending in the different body extremities (terminal points). Instead, the blood is first pumped through large-diameter arterial structures, which progressively branch out into smaller-diameter structures, finally ending in a fine web of tiny capillaries. Through the use of optimized, fractal-like, branching microchannel networks in heat sinks (Figure 10.14), she is able to achieve a 60% reduction in pressure drop

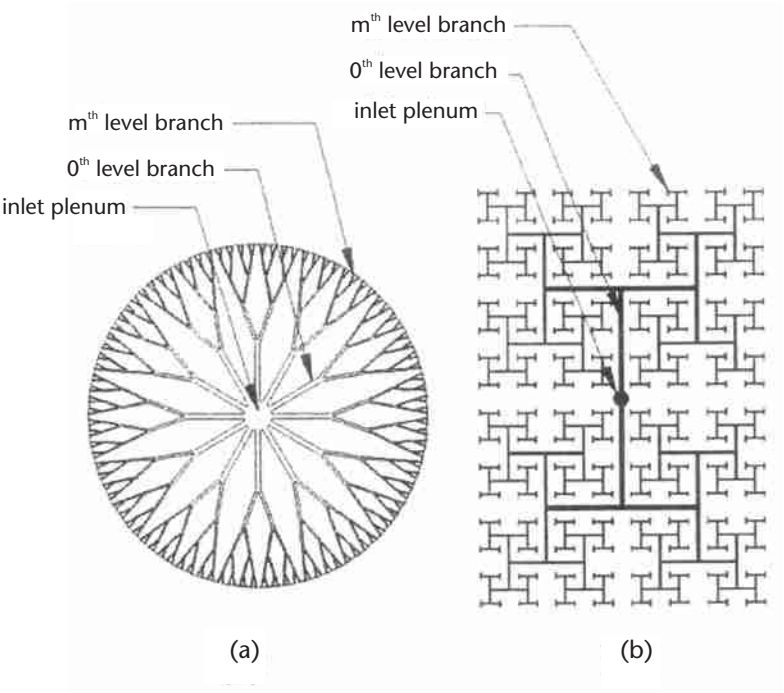

Figure 10.14 Fractal-like branching microchannel networks in heat sinks used in the study of Pence [48].

for the same flow rate and 30°C lower wall temperature under identical pumping-power conditions in comparison to the performance of an equivalent conventional parallel-microchannel heat sink arrangement. Enhanced thermal performance in a fractal-like microchannel branching network arises from the increase in convective heat-transfer coefficient associated with the smaller diameters and in the total number of developing entry regions resulting from the branching. This translates into lower average temperature and better temperature field uniformity. Wang et al. [49, 50] also advocate the use of tree-shaped and fractal-like microchannel nets for improved heat transfer and cooling for microelectronic chips. In addition to the thermal performance improvements, they emphasize the robustness of fractal-like networks as pertains to possible blockage of the fluid flow in the microchannels by particulate [50]. This is of particular importance in microelectronics cooling, which needs high reliability. They showed that tree-shaped microchannel networks were inherently more resilient to particle fouling, where a blocked channel results in the breakup of the system due to the increased temperature of the stagnant fluid, in comparison to straight microchannel networks. However, under very specific situations, the opposite might be true, especially if one of the main branches in the network were blocked, leading to major global failure.

It is evident that as the semiconductor industry moves toward 3-D IC, optimization of microchannel architectures becomes ever more important. Bejan's [47] three-quarters power law and minimum pumping-power optimization approach becomes even more relevant for these heat-generating volumetric systems and should be the block around which 3-D microchannel cooling architectures are devel-

oped. The work of Koo et al. [32] suggests that synergy between the chip and heat sink designers is crucial in order to achieve proper cooling of 3-D semiconductor chips. In general, the optimal cooling architecture should incorporate cues from all the previous optimization schemes, with cascading manifold microchannel networks that more closely resemble some of the 3-D examples found in nature, such as the respiratory and circulatory systems, river basins and deltas, and of course tree-branching morphology.

10.7 Future Outlook

Given the realm of cooling possibilities for microelectronic components, it is hard to predict what the future holds in terms of which technology will lead the way toward the cooling of 3-D ICs. In this chapter, we have concentrated on active microfluidic cooling solutions, specifically those based on convective flow through microchannels. If not a clear leading contender, this is one of the only promising technologies that has seen direct market application [51]. The reality is that with the current increases in microelectronics power densities, the envelope of this technology must be pushed in order to achieve the required heat-flux removal. Using the current benchmark for future cooling technologies of 1 kW/cm^2, we can expect that as the industry moves into 3-D architectures and the transistor size continues to decrease, volumetric cooling solutions will need to address dissipation of power densities on the order of at least 20 kW/cm^3. This will clearly require the development and implementation of very clever and novel cooling technologies. Microchannel convective cooling will most definitely have to rely on strategies that involve phase change and boiling, while addressing the issues associated with maintaining acceptable pressure-drop and pumping-power requirements, both of which become that much more challenging with the introduction of the increasing complexity associated with 3-D microchannel networks.

One of the major limitations associated with boiling microchannel systems is the proper management and disposal of the vapor phase. The sudden and explosive phase change that occurs in the microchannel has detrimental effects in terms of increased pressure drop, the onset of instabilities, and, most importantly, the occurrence of burnout and dryout conditions. To overcome these limitations, vapor-phase management solutions must be developed that enable taking advantage of the latent heat associated with phase change without incurring the negative effects. An extremely attractive solution is the use of local vapor-management devices that can quickly and efficiently remove the vapor phase at the phase-change location. One specific example of a very promising technology is the use of a vapor escape membrane developed by David et al. [52]. This device consists of a hydrophobic membrane located on top of the microchannel heat sink (Figure 10.15). The hydrophobic nature of the membrane permits venting of the vapor phase to an escape chamber, while preventing liquid passage to this vapor reservoir. This is effectively akin to a vapor-phase stripper, which maintains a fully liquid phase moving through the microchannels. As such, the issues associated with phase-change-acceleration pressure drop and burnout/dryout conditions are effectively eliminated.

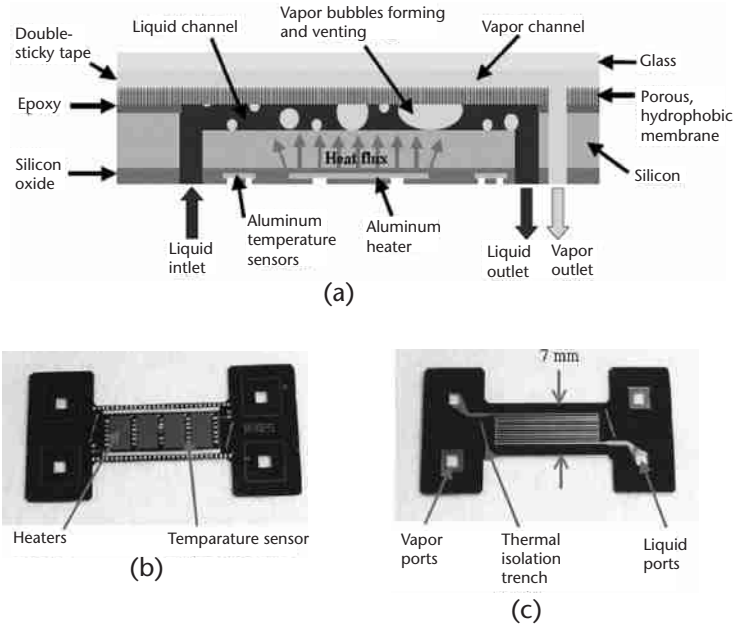

Figure 10.15 (a) Schematic of the vapor escape membrane concept being developed by David et al. [52]. The device consists of a hydrophobic membrane located on top of the microchannel heat sink. The hydrophobic nature of the membrane permits venting of the vapor phase to an escape chamber, while preventing liquid passage to this vapor reservoir. (b) Back side of the actual device, showing the integrated heaters and temperature sensors. (c) Front side of the actual device, showing the serpentine microchannel geometry.

10.8 Nomenclature

A_c	Microchannel cross-sectional area
A_p	Heat sink plenum cross-sectional area
C_f	Fanning friction-factor coefficient
$C_{f,app}$	Apparent Fanning friction-factor coefficient
c_p	Specific heat capacity at constant pressure
c_v	Specific heat capacity at constant volume
D	Circular microchannel internal diameter
D_h	Noncircular microchannel hydraulic diameter
f	Darcy friction-factor coefficient
h	Convective heat-transfer coefficient
K	Hagenbach's factor (incremental pressure-defect coefficient)
K_{90}	Hagenbach's factor for a 90° bend
K_c	Hagenbach's factor for a sudden contraction
K_e	Hagenbach's factor for a sudden expansion
k_f	Fluid thermal conductivity
L	Microchannel length
L_d	Chip die length
L_h	Hydrodynamic entry length
L_t	Thermal entry length
$\dot{m}$	Liquid mass flow rate
n	Direction normal to the microchannel wall surface
Nu	Nusselt number
p	Pressure

P	Perimeter
p_i	Inlet pressure
Po	Poiseuille number
p_o	Outlet pressure
Pr	Prandtl number
P_w	Wetted perimeter
Q	Liquid volume flow rate
q''_s	Surface heat flux
q_{conv}	Microchannel convective heat transfer
R	Circular microchannel internal radius
r	Circular microchannel radial coordinate
Re	Reynolds number
Re_D	Reynolds number based on circular microchannel internal diameter
Re_{Dh}	Reynolds number based on noncircular microchannel internal hydraulic diameter
T	Temperature
T_{char}	Characteristic temperature
$T_{f,i}$	Inlet fluid temperature
T_m	Mixed mean bulk-flow temperature
$T_{m,i}$	Inlet mixed mean bulk-flow temperature
$T_{m,o}$	Outlet mixed mean bulk-flow temperature
T_{max}	Maximum allowable chip die temperature
T_s	Microchannel wall surface temperature
u	Microchannel axial fluid velocity
u_{avg}	Average microchannel axial fluid velocity
w_c	Microchannel width
W_d	Chip die width
w_w	Microchannel wall width
x	Microchannel axial coordinate
x^+	Nondimensional microchannel axial coordinate
α	Rectangular microchannel aspect ratio
δ	Liquid-film thickness
ε	Surface roughness
μ	Fluid viscosity
μ_s	Fluid viscosity evaluated at the microchannel wall temperature
ρ	Fluid density
τ_w	Microchannel wall shear stress

References

[1] Kandlikar, S. G., and A. V. Bapat, "Evaluation of Jet Impingement, Spray and Microchannel Chip Cooling Options for High Heat Flux Removal," *Heat Transfer Engineering,* Vol. 28, No. 11, 2007, pp. 911–923.

[2] Tuckerman, D. B., and R. F. W. Pease, "High-Performance Heat Sinking for VLSI," *IEEE Electron Device Letters,* Vol. 2, No. 5, 1981, pp. 126–129.

[3] Phillips, R. J., "Forced-Convection, Liquid-Cooled, Microchannel Heat Sinks," MSME Thesis, Cambridge, 1987.

[4] Samalam, V., "Convective Heat Transfer in Microchannels," *J. Electronic Materials,* Vol. 18, No. 5, 1989, pp. 611–617.

[5] Peng, X. F., and B. X. Wang, "Forced Convection and Flow Boiling Heat Transfer for Liquid Flowing through Microchannels," *Int. J. Heat and Mass Transfer,* Vol. 36, No. 14, 1993, pp. 3421–3427.

[6] Bowers, M. B., and I. Mudawar, "High Flux Boiling in Low Flow Rate, Low Pressure Drop Mini-Channel and Micro-Channel Heat Sinks," *Int. J. Heat and Mass Transfer,* Vol. 37, No. 2, 1994, pp. 321–332.

[7] Peles, Y. P., L. P. Yarin, and G. Hetsroni, "Heat Transfer of Two-Phase Flow in a Heated Capillary," *Proc. 11th International Heat Transfer Conference*, Kuongju, Korea, **<AQ: date?>**1998, pp. 193–198.

[8] Lin, S., P. A. Kew, and K. Cornwell, "Two-Phase Heat Transfer to a Refrigerant in a 1 mm Diameter Tube," *Int. J. Refrigeration,* Vol. 24, No. 1, 2001, pp. 51–56.

[9] Qu, W., and I. Mudawar, "Experimental and Numerical Study of Pressure Drop and Heat Transfer in a Single-Phase Micro-Channel Heat Sink," *Int. J. Heat and Mass Transfer,* Vol. 45, No. 12, 2002, pp. 2549–2565.

[10] Zhang, L., et al., "Measurements and Modeling of Two-Phase Flow in Microchannels with Nearly Constant Heat Flux Boundary Conditions," *J. Microelectromechanical Systems,* Vol. 11, No. 1, 2002, pp. 12–19.

[11] Agostini, B., et al., "State of the Art of High Heat Flux Cooling Technologies," *Heat Transfer Engineering,* Vol. 28, No. 4, 2007, pp. 258–281.

[12] Goodling, J. S., "Microchannel Heat Exchangers: A Review," **<AQ: Journal/proc. title?>**San Diego, California, 1993, pp. 66–82.

[13] Hassan, I., P. Phutthavong, and M. Abdelgawad, "Microchannel Heat Sinks: An Overview of the State-of-the-Art," *Microscale Thermophysical Engineering,* Vol. 8, No. 3, 2004, pp. 183–205.

[14] Hidrovo, C. H., et al., "Two-Phase Microfluidics for Semiconductor Circuits and Fuel Cells," *Heat Transfer Engineering,* Vol. 27, No. 4, 2006, pp. 53–63.

[15] Gad-el-Hak, M., "Fluid Mechanics of Microdevices—The Freeman Scholar Lecture," *J. Fluids Engineering, Transactions of the ASME,* Vol. 121, No. 1, 1999, pp. 5–33.

[16] Colin, S., "Single-Phase Gas Flow in Microchannels," *Heat Transfer and Fluid Flow in Minichannels and Microchannels*, **<AQ: city of publication?>**Elsevier, 2006, pp. 9–86.

[17] Shah, R. K., and A. L. London, *Advances in Heat Transfer. Laminar Flow Forced Convection in Ducts. A Source Book for Compact Heat Exchanger Analytical Data*, New York: Academic Press, 1978.

[18] Kandlikar, S. G., "Single-Phase Liquid Flow in Minichannels and Microchannels," *Heat Transfer and Fluid Flow in Minichannels and Microchannels*, **<AQ: city of publication?>**Elsevier, 2006, pp. 87–136.

[19] Chen, R. Y., "Flow in the Entrance Region at Low Reynolds Numbers," *J. Applied Mechanics, Transactions ASME*, Vol. 95, No. 1, 1973, pp. 153–158.

[20] White, F. M., *Fluid Mechanics*, 6th ed., New York: McGraw-Hill, 2008.

[21] Incropera, F. P., et al., *Fundamentals of Heat and Mass Transfer*, 6th ed., New York: John Wiley & Sons, 2007.

[22] Qu, W., and I. Mudawar, "Measurement and Prediction of Pressure Drop in Two-Phase Micro-Channel Heat Sinks," *Int. J. Heat and Mass Transfer,* Vol. 46, No. 15, 2003, pp. 2737–2753.

[23] Kandlikar, S. G., et al., "High-Speed Photographic Observation of Flow Boiling of Water in Parallel Mini-Channels," **<AQ: journal title?>**Anaheim, California, 2001, pp. 675–684.

[24] Hetsroni, G., et al., "A Uniform Temperature Heat Sink for Cooling of Electronic Devices," *Int. J. Heat and Mass Transfer,* Vol. 45, No. 16, 2002, pp. 3275–3286.

[25] Peles, Y. P., L. P. Yarin, and G. Hetsroni, "Steady and Unsteady Flow in a Heated Capillary," *Int. J. Multiphase Flow,* Vol. 27, 2001, pp. 577–598.

[26] Xu, J., J. Zhou, and Y. Gan, "Static and Dynamic Flow Instability of a Parallel Microchannel Heat Sink at High Heat Fluxes," *Energy Conversion and Management,* Vol. 46, No. 2, 2005, pp. 313–334.

[27] Chang, K. H., and C. Pan, "Two-Phase Flow Instability for Boiling in a Microchannel Heat Sink," *Int. J. Heat and Mass Transfer,* Vol. 50, No. 11–12, 2007, pp. 2078–2088.

[28] Koo, J.-M., et al., "Convective Boiling in Microchannel Heat Sinks with Spatially-Varying Heat Generation," **<AQ: journal title?>**San Diego, California, 2002, pp. 341–346.

[29] Koo, J.-M., et al., "Modeling of Two-Phase Microchannel Heat Sinks for VLSI Chips," **<AQ: journal title?>**Interlaken, Switzerland, **<AQ: date?>**2001, pp. 422–426.

[30] Qu, W., and I. Mudawar, "Flow Boiling Heat Transfer in Two-Phase Micro-Channel Heat sinks—II. Annular Two-Phase Flow Model," *Int. J. Heat and Mass Transfer,* Vol. 46, No. 15, 2003, pp. 2773–2784.

[31] Kleinstreuer, C., *Two-Phase Flow: Theory and Applications*, New York: Taylor & Francis, 2003.

[32] Koo, J.-M., et al., "Integrated Microchannel Cooling for Three-Dimensional Electronic Circuit Architectures," *J. Heat Transfer,* Vol. 127, No. 1, 2005, pp. 49–58.

[33] Kandlikar, S. G., "General Correlation for Saturated Two-Phase Flow Boiling Heat Transfer inside Horizontal and Vertical Tubes," *J. Heat Transfer, Transactions ASME,* Vol. 112, No. 1, 1990, pp. 219–228.

[34] Levy, S., *Two-Phase Flow in Complex Systems*, New York: John Wiley & Sons, 1999.

[35] Brennen, C. E., *Fundamentals of Multiphase Flow*, Cambridge: Cambridge University Press, 2005.

[36] Garimella, S., J. D. Killion, and J. W. Coleman, "Experimentally Validated Model for Two-Phase Pressure Drop in the Intermittent Flow Regime for Circular Microchannels," *J. Fluids Engineering, Transactions of the ASME,* Vol. 124, No. 1, 2002, pp. 205–214.

[37] Suo, M., and P. Griffith, "Two-Phase Flow in Capillary Tubes," *American Society of Mechanical Engineers—Transactions—J. Basic Engineering,* Vol. 86, No. 3, 1964, pp. 576–582.

[38] Fukano, T., A. Kariyasaki, and M. Kagawa, "Flow Patterns and Pressure Drop in Isothermal Gas-Liquid Concurrent Flow in a Horizontal Capillary Tube," *Nippon Kikai Gakkai Ronbunshu, B Hen/Transactions of the Japan Society of Mechanical Engineers, Part B,* Vol. 56, No. 528, 1990, pp. 2318–2325.

[39] Garimella, S. V., and V. Singhal, "Single-Phase Flow and Heat Transport and Pumping Considerations in Microchannel Heat Sinks," *Heat Transfer Engineering,* Vol. 25, No. 1, 2004, pp. 15–25.

[40] Singhal, V., D. Liu, and S. V. Garimella, "Analysis of Pumping Requirements for Microchannel Cooling Systems," **<AQ: journal?>**Maui, Hawaii, **<AQ: date?>**2003, pp. 473–479.

[41] Wei, X., and Y. Joshi, "Optimization Study of Stacked Micro-Channel Heat Sinks for Micro-Electronic Cooling," *IEEE Transactions on Components and Packaging Technologies,* Vol. 26, No. 1, 2003, pp. 55–61.

[42] Wei, X., and Y. Joshi, "Stacked Microchannel Heat Sinks for Liquid Cooling of Microelectronic Components," *J. Electronic Packaging, Transactions of the ASME,* Vol. 126, No. 1, 2004, pp. 60–66.

[43] Harpole, G. M., and J. E. Eninger, "Micro-Channel Heat Exchanger Optimization," **<AQ: journal title?>**Phoenix, Arizona, **<AQ: date?>**1991, pp. 59–63.

[44] Copeland, D., "Manifold Microchannel Heat Sinks: Analysis and Optimization," *Thermal Science Engineering,* Vol. 3, No. 1, 1995, pp. 7–12.

[45] Copeland, D., M. Behnia, and W. Nakayama, "Manifold Microchannel Heat Sinks: Isothermal Analysis," *IEEE Transactions on Components, Packaging, and Manufacturing Technology Part A,* Vol. 20, No. 2, 1997, pp. 96–102.

[46] Gosselin, L., and A. Bejan, "Tree Networks for Minimal Pumping Power," *Int. J. Thermal Sciences,* Vol. 44, No. 1, 2005, pp. 53–63.

[47] Bejan, A., "The Tree of Convective Heat Streams: Its Thermal Insulation Function and the Predicted 3/4-Power Relation between Body Heat Loss and Body Size," *Int. J. Heat and Mass Transfer,* Vol. 44, No. 4, 2001, pp. 699–704.

[48] Pence, D. V., "Reduced Pumping Power and Wall Temperature in Microchannel Heat Sinks with Fractal-Like Branching Channel Networks," *Microscale Thermophysical Engineering,* Vol. 6, No. 4, 2002, pp. 319–330.

[49] Wang, X.-Q., A. S. Mujumdar, and C. Yap, "Thermal Characteristics of Tree-Shaped Microchannel Nets for Cooling of a Rectangular Heat Sink," *Int. J. Thermal Sciences,* Vol. 45, No. 11, 2006, pp. 1103–1112.

[50] Wang, X.-Q., A. S. Mujumdar, and C. Yap, "Numerical Analysis of Blockage and Optimization of Heat Transfer Performance of Fractal-Like Microchannel Nets," *J. Electronic Packaging, Transactions of the ASME,* Vol. 128, No. 1, 2006, pp. 38–45.

[51] Upadhya, G., et al., "Micro-Scale Liquid Cooling System for High Heat Flux Processor Cooling Applications," **<AQ: journal title?>**Dallas, Texas, **<AQ: date?>**2006, pp. 116–119.

[52] David, M. P., et al., "Vapor-Venting, Micromachined Heat Exchanger for Electronics Cooling," *Proc. IMECE2007: 2007 ASME International Mechanical Engineering Congress and Exposition*, Seattle, Washington, **<AQ: date?>**2007.**<AQ: pages?>**